DEVELOPMENT OF A THERMOMECHANICAL FINITE ELEMENT MODEL FOR LASER POWDER BED FUSION PROCESS AND ITS COMPARISON WITH INHERENT STRAIN METHOD

by
CAN BAYRAKTAR

Submitted to the Graduate School of Engineering and Natural Sciences
in partial fulfilment of
the requirements for the degree of
Master of Science

Sabancı University
June 2021

DEVELOPMENT OF A THERMOMECHANICAL FINITE ELEMENT MODEL FOR LASER POWDER BED FUSION PROCESS AND ITS COMPARISON WITH INHERENT STRAIN METHOD

APPROVED BY:

DATE OF APPROVAL: 08/06/2021

ABSTRACT

DEVELOPMENT OF A THERMOMECHANICAL FINITE ELEMENT MODEL FOR LASER POWDER BED FUSION PROCESS AND ITS COMPARISON WITH INHERENT STRAIN METHOD

CAN BAYRAKTAR

MANUFACTURING ENGINEERING M.Sc. THESIS, JUNE 2021

Thesis Supervisor: Asst. Prof. Dr. Eralp Demir

Keywords: process modeling, finite element method, laser powder bed fusion, residual stresses, inherent strain method, additive manufacturing

The Laser Powder Bed Fusion process as an additive manufacturing method is used for layer-by-layer production of metal components. In recent years, the process has attracted great attention from industries such as aerospace and automotive because of its ability to produce parts with complex geometries from materials with low machinability. However, residual stresses that build up during the process due to high thermal gradients negatively affect the overall quality and mechanical performance of the end product. Hence, further investigation is needed on the relationship between process parameters and residual stresses.

In this study, a thermomechanical finite element model was developed for the estimation of thermal history and residual stresses by simulating the LPBF process. A commercial finite element software was used in combination with user-defined subroutines. A methodology was implemented to the thermomechanical model to express surface heat losses as a volumetric heat loss using Gauss' theorem. This method eliminated the need to repeatedly define free surfaces after deposition of each layer.

The model predicted the melt pool dimensions with a less than %10 error according to the experimental data. A parametric study was carried out to observe the impact of process parameters and scan pattern on melt pool size, maximum temperature and residual stresses. From the theory of inherent strain, a stress-based variant was developed to estimate stresses directly from a thermal solution. The developed method predicted the stresses with a maximum of %15 deviation in comparison to the thermomechanical solution and also computational time was decreased by six times.

ÖZET

LAZER TOZ YATAKLI KAYNAŞTIRMA SÜRECİNİN SONLU ELEMAN YÖNTEMİ İLE TERMOMEKANİK MODELLENMESİ VE ÖZ GERİNİM YÖNTEMİ İLE KARŞILAŞTIRILMASI

CAN BAYRAKTAR

ÜRETİM MÜHENDİSLİĞİ YÜKSEK LİSANS TEZİ, HAZİRAN 2021

Tez Danışmanı: Dr. Öğr. Üyesi Eralp Demir

Anahtar Kelimeler: proses modelleme, , sonlu eleman yöntemi, lazer toz yataklı kaynaştırma süreci, kalıntı gerilimler, öz gerinim yöntemi, eklemeli üretim

Lazer toz yataklı kaynaştırma süreci bir eklemeli üretim yöntemi olup metal parçaların katmanlar şeklinde imalatında kullanılır. Süreç, karmaşık geometrilere ve işlenebilirliği düşük malzemelere sahip parçaların imal edebilmesi sayesinde özellikle son yıllarda havacılık ve otomotiv endüstrileri tarafından dikkat çekmiştir. Ancak, süreç esnasında yüksek sıcaklık farklarından dolaylı oluşan kalıntı gerilimler, üretilen parçaların kalitesini ve mekanik performasını olumsuz yönde etkilemektedir. Dolayısıyla kalıntı gerilimlerin süreç parametreleri ile ilişkisinin daha fazla araştırılmasına ihtiyaç duyulmaktadır.

Bu çalışmada, lazer toz yataklı kaynaştırma süreci simüle edilerek termal geçmiş ve kalıntı gerilmelerin tahmini için bir termomekanik sonlu eleman modeli geliştirilmiştir. Bunun için kullanıcı tanımlı alt rutinler ile birlikte bir ticari sonlu eleman yazılımı kullanılmıştır. Gauss teoremi kullanılarak geliştirilen bir yöntem, yüzey ısı kayıplarının hacimsel ısı kaybı olarak hesaplanbilmesi sağlanmıştır. Bu yöntem ile açık yüzeylerin her katmanda yeniden tanımlanması gereksimi ortadan kaldırılmıştır.

Termomekanik model, eriyik havuzu boyutlarını deneysel sonuçlara göre %10'dan az hata ile hesaplamıştır. Parametrik bir çalışma ile süreç parametrelerinin eriyik havuz boyutlarına, sıcaklıklara, ve kalıntı gerilimlere etkisi incelenmiştir. Öz gerinim teorisinin gerilim bazlı olarak yeniden formüle edilmesiyle geliştirilen yöntem, kalıntı gerilimlerin sadece termal çözümü kullanarak hesaplanabilmesini sağlamıştır. Bu yöntem kalıntı gerilimleri termomekanik analiz sonuçlarına kıyasyla en fazla %15 sapma ile tahmin etmiştir. Ayrıca hesaplama süresi altı kat azaltılmıştır.

ACKNOWLEDGMENTS

First of all, I would like to thank my advisor Assist. Prof. Dr. Eralp Demir. He has been a mentor to me beyond an academic advisor. It is because of him that I got the skills and knowledge that I have now. He was always encouraging, supportive and kind. I could not have achieved this degree without his guidance.

I would like to thank my dear friends and colleagues; Beril Çetin, Kerem Dörtkaşlı, Ali Rasheed, Sina Khalilvandi, and Mohammad Joudivand for their friendship and support during my studies.

I would also like to thank the members of our research center; project engineer and researcher Dr. Murat Işık, technical manager Ragıp Orkun Seçer, laboratory technicians Fatih Polat and Ömer Altıntaş for their efforts during my experimental studies.

Faculty members of our university; Prof. Dr. Bahattin Koç, Prof. Dr. Mehmet Yıldız, Prof. Dr. Erhan Budak, and Assist. Prof. Dr. Taner Tunç have always provided their knowledge and experience through their excellent courses. I am so grateful to have the chance to take their courses.

Dedicated to my dearest family

TABLE OF CONTENTS

LIST OF TABLES

LIST OF FIGURES

LIST OF ABBREVIATONS

AM	Additive manufacturing
BCs	Boundary conditions
CFD	Computational Fluid Dynamics
CAD	Computer-aided design
DMLS	Direct Metal Laser Sintering
DED	Directed Energy Deposition
EPBF	Electron Beam Powder Bed Fusion
FE	Finite element
FEM	Finite element method
FDM	Fused Deposition Modeling
HAZ	Heat-affected zone
ISM	Inherent strain method
LOM	Laminated Object Manufacturing
LPBF	Laser Powder Bed Fusion
LHS	Left-hand side
RHS	Right-hand side
RS	Residual stresses
SLM	Selective Laser Melting
SLS	Selective Laser Sintering
SSPT	Solid-state phase transformation
SL	Stereolithography

LIST OF SYMBOLS

α	thermal expansion coefficient
β	constraint coefficient
Δd	hatch spacing
ΔH_v^*	effective enthalpy of metal vapor
Δh	layer thickness
Δp	plastic strain increment
Δt_{dwell}	time step during the dwell time interval
Δt_{recoat}	time step during the recoating time interval
Δt_{scan}	time step during the scan time interval
$\varepsilon^{(H)}$	emissivity of the powder surface vacancies
$\varepsilon^{(p)}$	emissivity of powder
$\varepsilon^{(s)}$	emissivity of solid
ϵ_{IS}	inherent strain
ϵ	total strain
$\epsilon_{elastic}$	elastic strain
$\epsilon_{plastic}$	plastic strain
$\epsilon_{thermal}$	thermal strain
ζ	ratio of the solid conductivity to Argon gas's
η	absorptivity
ρ	mass density
$\rho^{(p)}$	powder density
σ_{VM}	Von-Mises stress

σ_{xx}^{*}	normalized longitudinal stress
σ_{yy}^{*}	normalized transverse stress
ν	Poisson's ratio
φ	porosity
ψ	yield function
$\dot{q}_{loss}$	total heat losses from surface
$\dot{Q}$	heat input
$\widehat{\mathbf{T}}$	temperatures at the nodes
$\widehat{\mathbf{T}}_{\boldsymbol{t}}$	temperatures at the nodes at former time increment
$\widehat{\mathbf{u}}$	displacements at the nodes
$\mathbf{x_s}$	position on the surface
B	stress-displacement matrix
C	elasticity matrix
$\mathbf{C_p}$	heat capacitance matrix
F	total force acting on a body
k	conductivity matrix
n	area normal
$\mathbf{n_p}$	plastic flow direction
N	interpolation function
q	heat flux vector
t	traction
v	velocity vector
I	identity matrix
R	residual force vector

$\mathbf{R}_E$	external load vector
$\mathbf{S}$	residual stress
$\mathbf{u}$	displacements
$\mathbf{x}$	position in 3-dimenisonal space
$\boldsymbol{\kappa}$	internal force vector
$\boldsymbol{\sigma}$	stress
$\boldsymbol{\sigma}'$	deviatoric stress
a	scaling factor
A, As, C	constants used in inherent strain & stress calculation
$A^{(H)}$	porous area fraction of powders
b	body forces
C_p	solid liquid specific heat
$C_p^{(p)}$	powder specific heat
e	minimum elements size in scan direction
E	modulus of elasticity
$E^{(p)}$	modulus of elasticity of powder
$f^{(s)}$	solid fraction
f_0	calibration factor
h	convection coefficient
$k^{(Ar)}$	conductivity of argon gas
$k^{(p)}$	conductivity of powder
K_B	Boltzmann constant
L_0	scan vector length
L^*	normalized scan vector length

M	molar mass of metal vapor
P	laser power
R	universal gas constant
r_x, r_y	radii of the laser beam
r_0	the maximum beam diameter
r_z	penetration depth
S	surface of the domain
T	temperature
T_v	boiling temperature
T_s	surface temperature
T_1, T_2	temperature limits
T_0	ambient temperature
t	time
$t_{\text{scan time}}$	time for deposition of a single scan track
t_{layer}	time for deposition of a single layer

1 INTRODUCTION

The definition of additive manufacturing (AM) is given as the "joining of materials layer upon layer to make parts from 3-dimensional model data" by the standard ISO/ASTM 52900:2015 [1]. Attention and demand for AM technologies have been significantly increased within the last few decades especially in the fields of biomedical, aerospace, and automotive due to their advantages. One of the greatest benefits of additive manufacturing is the design freedom that it provides with extending the constraints of conventional manufacturing techniques [2]. Innovative complex designs, including algorithm-based design, increase the functionality of the component by allowing to produce customizable products. Moreover, with the design optimization techniques such as topology optimization, significant weight reduction is possible with AM [3]. Additional to that, a very important feature of AM is the elimination of costly and time-consuming process planning stages in the development stage such as tool and mold preparation. This gives the flexibility to produce parts with various geometries and sizes for different applications with a single machine and tool. Therefore, gathering the prototype directly from the computer-aided design (CAD) file makes the iterative design procedure much faster and less costly [4]. Another important benefit is drastic material waste reduction considering both economic and environmental concerns. Since during manufacturing most of the aerospace components with milling process, up to around 75% percent to 95% of material is getting machined [5]. Certainly, AM also has some downsides, such as long manufacturing times, post-process requirements, support structures, optimization of process parameters, residual stress. Latter were the main subjects of this study, hence further discussion is made in the upcoming sections. The major advantages and challenges of AM are summarized in Table 1-1 [5], [6].

Table 1-1: Advantages and disadvantages of AM [5], [6].

Advantages	Challenges
• Design flexibility	• High production time
• Material waste reduction	• Cost of the production
• Elimination of tooling	• Post-process requirements
• Rapid prototype development	• Process parameter optimization
• Customizable products	• Size limitations
• Lightweight design	• Support requirement

Stereolithography (SL) was the first commercially available additive manufacturing technology that was introduced back in the late-1980s by 3D Systems. In SL technology or classified as Vat Photopolymerization process, photopolymers are cured with the applied radiation coming from ultraviolet or visibly light. SL remained the only modern commercial AM technology until 1991 when other AM technologies such as Fused Deposition Modeling (FDM) and Laminated Object Manufacturing (LOM) were introduced to commercial use that are classified as extrusion-based and sheet lamination processes respectively. These had been followed by the first Powder Bed Fusion technology; Selective Laser Sintering (SLS) in 1992, where powder form of the materials is used with a laser heat source. This technology was mainly to manufacture plastic products, but it was advanced to process different materials such as metals and ceramics in the following years. In early 2000, direct metal deposition technology also known as the Directed Energy Deposition (DED) process was released. In DED, the powder material is melted and deposited simultaneously while exiting from the nozzle. Relatively large parts can be manufactured and also repairing the parts is possible. Hybrid DED machines are available that combines machining with additive manufacturing. The categorization of AM processes according to Gibson et al. is shown in Figure 1-1 [7], [8].

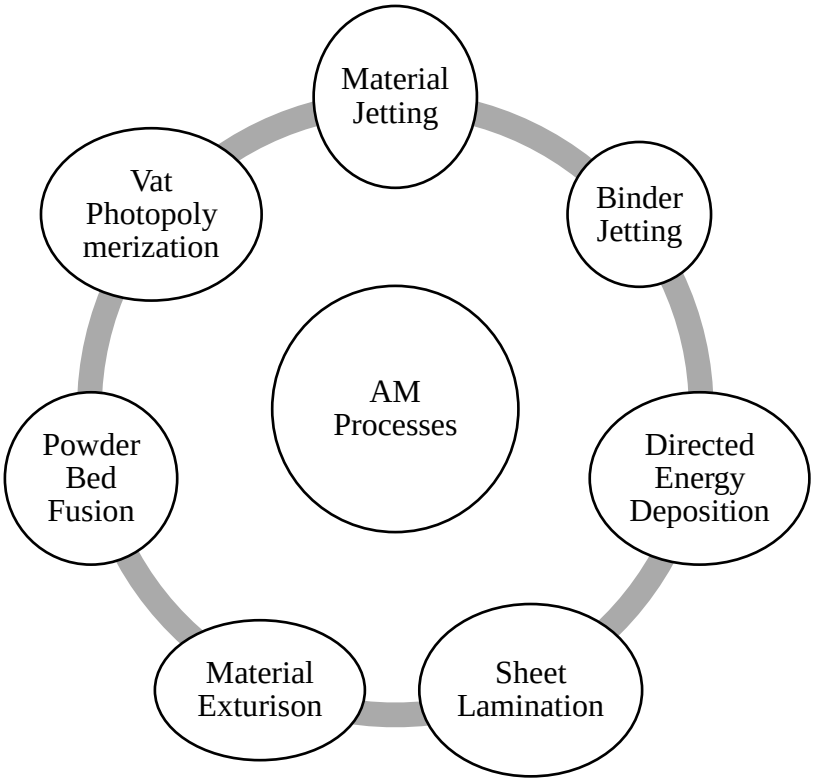

Figure 1-1 Classification of AM processes.

1.1 Powder Bed Fusion process for metals

As mentioned earlier, Powder Bed Fusion uses powder forms of materials in a bed and with a heat source selectively sinter or melt them to depose the desired geometrical pattern within a layer. After a layer is deposited, another layer of powder is put on the bed, and this operation is continued until the entire piece has been deposited. The process distinguishes depending on the material that is processed, whether polymer or metal. In metal deposition without any binding, generally, the material is fully melted via electron or laser beam. Nickel-based, titanium, or steel alloys are mostly used metal powders. The enclosed atmosphere in Laser Powder Bed Fusion (LPBF) is filled with argon or nitrogen gas, wherein the Electron Beam Powder Bed Fusion (EPBF), is almost vacuum. For pre-heating of the powder, EPBF uses the defocused electron-beam, whereas in LPBF baseplate underneath the powder bed is pre-heated by resistive heating [7], [9].

1.2 Laser Powder Bed Fusion (LPBF) process

The AM technologies such as Direct Metal Laser Sintering (DMLS), Selective Laser Melting (SLM), or LaserCusing are commercial names for the pretty much same process where powder form of metal alloys is melted via a laser heat source and deposition is completed by solidification of the material. In this study, the term Laser Powder Bed Fusion (LPBF) is used to refer to this process. Currently, LPBF is one of the most popular AM methods for producing metal parts due to its benefits [9]. By contrast to $C0_2$ lasers that are used in the SLS process, Yb-fiber lasers are often preferred because of the absorptivity concern for metal powder. The process is highly automated, the only manual operations required are placing baseplate and adjusting recoating blade before the process and removing the part from the baseplate after the process. Powder layers are spread by an automated recoating blade with a prescribed thickness, that is mostly around 20-100 μm to increase the resolution while the baseplate is lowered with the same amount. The build chamber is filled with argon gas. Oxygen level and pressure are kept under control during the process to prevent oxidation. Parts with high mechanical properties such as yield strength, ultimate tensile strength with relative densities up to %99.9 can be achievable [10], [11]. Laser beam power, scan speed, hatch spacing, layer thickness, and scan strategy are major common parameters for the process. Certainly, depending on the commercial technology, each may have other specific parameters.

Besides the advantages, there are several challenges that the LPBF process has, such as the requirement of a support structure, long part construction time due to pre and post-processes, the occurrence of high residual stresses (RS), and geometrical distortions. As a result of high thermal gradients and rapid cooling rates during the process, anisotropic residual stresses are formed that negatively affect the mechanical performance of the deposited component. This is the main focus of this study, hence further discussion is made in the following sections. Additionally, the same mechanism of forming RS results in unwanted geometrical distortions. The magnitude and isotropy of RS are dependent on the process parameters that are mentioned above. Considering that the LPBF process is quite recent compared to conventional manufacturing methods, relationship between process parameters and RS still requires research and understanding.

1.3 Residual stresses in LPBF process

The definition of residual stresses is stresses that are left within material without the existence of any external load even though part is in equilibrium. The cause of these stresses is usually plastic deformation that occurs in a non-homogeneous way. During most of the manufacturing processes, residual stresses are formed [12]. Development of tensile RS on the surface would affect the fatigue behavior of the material negatively by contributing to crack propagation which causes failure. By contrast, compressive RS may prevent crack forming and increase fatigue performance. However, in welding and LPBF processes, residual stresses are tried to be minimized. During the LPBF process, high intensity localized heat source causes generation of high thermal gradients within the material, additionally considerably low conductivity of powder prevents uniform dissipation of the heat through conduction. The finished workpiece contains high RS due to rapid heating and cooling with thermal expansion and contraction cycles. During heating, the melt pool expands compresses the material underneath. Then, while the melt pool cools down, it shrinks but due to the surrounded material acts as a mechanical constraint, high tensile stresses occur. The residual stresses are often classified as Type I, II, and III. Type II and Type III residual stresses are in microstructural and atomic scale, generally resultant due to phase differences and microstructural dislocations. Hence, for the LPBF process, generally significant one is Type I residual stresses that influence the strength and fatigue life of the material directly [13], [14].

The residual stresses and geometrical distortions are major downsides of the LPBF process. Pre-heating the baseplate or post-process applications such as heat treatment are possible to reduce RS within the finished part, which consequently increases production time and cost. Moreover, support structures are often used to prevent warping and distortion to some extent. Support structure requirement increases the complexity of the process, and also needs time consuming post-processes. Additionally, in extreme RS forming, failure may occur even during the process with crack openings on the surface. Hence, reduction and distribution of RS in the LPBF process are crucial to increase the mechanical performance of the product and decrease the post-process requirements at the same time.

1.4 Numerical modeling of LPBF process

As a relatively recent technology, powder-based additive manufacturing method, LPBF, is still open to further research on understanding influence of baseplate and part material, part geometry, process parameters on the performance and quality of the finished workpiece. As mentioned before, process parameters including scanning strategy may play an important role in the mechanical performance and properties of the end product by affecting RS and distortion generation. The experimental trial-error methods are possible for analyzing RS development during the process, however, they are costly and time consuming. As a result, computational modeling of the LPBF process can be used in the prediction of residual stresses that are left in the final product by simulating the process. Also, models would be useful in understanding the process mechanism and optimization of the process parameters accordingly. Computational models can be used to simulate thermal behavior during the process such as temperature history, melt pool geometry, and even fluid dynamics within the melt pool [15]. Moreover, microstructure, detailed phase change mechanism, RS, and distortion development can be modeled as well. However, complex interactions between melt-pool and surroundings, temperature-dependent properties, and wide range of temperature variation, localized relatively small laser beam diameter, phase change mechanism are computationally costly considerations and making modeling process a challenging task.

In this section, different modeling approaches with varying domain sizes and also efforts on the heat source and material modeling are discussed. Moreover, investigations on the influence of material properties, part geometry, process parameters, and scan strategies on the RS development are discussed with a literature review. Moreover, welding simulations are introduced briefly, since they are the origin of LPBF modeling due to similarities such as intense heat source, rapid heating and cooling cycles, and forming of thermally induced residual stresses.

1.4.1 Background: Welding Simulations

To understand the thermomechanical mechanism behind the welding processes and predict microstructural and mechanical properties, computational models were started to be developed in the early 1970s. In the actual process, there is a coupling between thermal and mechanical interaction since mechanical deformations would end up the generation of heat energy that consequently affects thermal solution. However, in most of the models, analyses were done in a decoupled fashion, where the thermal analysis was solved first and the output of it was used as an input for a mechanical analysis for each time-step. Yet, some detailed models were using coupled solving procedures, even though they were not common. One of the first heat source modeling efforts was done by Rosenthal, where an analytical moving point heat source on the surface was modelled to predict temperature distribution of heat-affected zone (HAZ). However, temperature prediction close to the point source was not accurate [16]. Then it was developed further as a 2-dimensional surface source by the same researcher. These were followed by point, surface, and 3-dimensional Gaussian heat source models.

Finite element method is one of the most commonly used numerical methods for AM simulations, although there are studies that use finite difference or volume methods. Investigations over the melt pool geometry were made through transient flow models. Additional to that, studies that model flow dynamics within the keyhole are present. Prediction of thermal history is significant to decide on welding process parameters [17]. Moreover, mechanical 2-D or 3-D models are used in the estimation of residual stress and geometrical distortion [18].

Modeling efforts that were done for welding processes guided researchers while developing LPBF process simulations, since they have common features as high thermal gradients, phase change and solidification, RS, and distortion mechanism. However, the LPBF process has distinctions and requires further considerations such as low conductivity powder, various scan strategies, longer process time, and deposition mechanism that adds up the complexity and computational cost of the models.

1.4.2 Heat source modeling

The heat source of the laser beam in the LPBF process is one of the fundamental considerations in a model. Temperature distribution, melt pool geometry, and even deposited region geometry will be influenced by the heat source. Usually, surface or volumetric heat sources were used by the researchers depending on the desired accuracy and scale of the model. The Gaussian distribution is one of the most common ways to represent the laser beam in the LPBF process. In equation (1-1), P is the laser power, η, absorptivity r_0, the maximum beam diameter. In this formulation heat source is modeled as surface heat flux over the top surface without any depth penetration. To consider the laser penetration into the material, Gaussian distribution can have the form that is shown as equation (1-2) [19], with a semi-spherical volumetric representation, where x', y' and z' are the distances from the center of the laser beam in each axis. As it is done for equation (1-2), the Gaussian distribution model can be modified to various geometries such as semi-ellipsoidal and conical or cylindrical. Additional to these, there are models that top surface is again represented as Gaussian distribution but along the depth, it is a function of the z-axis which is called the absorptivity profile function. This function can be based on analytical or numerical formulations.

$$q(x,y) = \frac{2\eta P}{\pi r_0^2} \exp\left(-2\frac{x'^2 + y'^2}{r_0}\right) \tag{1-1}$$

$$q(x,y,z) = \frac{2^{\frac{5}{2}}\eta P}{\pi^{\frac{3}{2}} r_0^3} \exp\left(-2\frac{x'^2 + y'^2 + z'^2}{r_0}\right) \tag{1-2}$$

Additionally, since these models require fine mesh and time-step resolution, further modifications and assumptions were made to be used especially in macro-scale simulations. Irwin et al.[20] proposed two heat input models that were line and elongated-ellipsoid methods, that allowed to use higher number of timesteps and decrease computational time.

1.4.3 Material modeling

To accurately simulate the LPBF process temperature dependence of the material properties should be considered since during the process wide temperature variation occurs within the material. Moreover, three different phases of the material are present as the powder, liquid, and solid, and their properties alter significantly. There are various formulations to relate the properties of powder with the bulk. One simple method is using only the porosity, φ, as it is shown in equation (1-3), where $k^{(s)}$and $k^{(p)}$ are conductivities of solid and powder phases respectively. The porosity value is often used to relate the other parameters such as density, specific heat, and emissivity. More accurate different correlations are also available using the porosity value as shown in equation (1-4) [21]. Additional to these, there are more detailed formulations that put into consideration of conductivity of surrounding argon gas, radiative heat transfer between powder particles, and also powder particle diameter. These formulations generally calculate powder conductivity as %1-%10 of the bulk material. To account for Marangoni convection within the melt pool, considerations such as increased convection coefficient or artificial modifications can be done to the conduction coefficient.

$$k^{(p)} = (1-\varphi)k^{(s)} \tag{1-3}$$

$$k^{(p)} = \frac{(1-\varphi)}{1+11\varphi^2}k^{(s)} \tag{1-4}$$

Another challenge is to predict mechanical properties such as elastic modulus and yield strength at the liquid and powder phases, because of the experimental difficulties. Certain assumptions are often made by the researchers to overcome that. Zhao et al. [22] neglected elastic modulus and yield strength of the material in the powder phase. While Parry et al. [23] used a factor of 0.1 for elastic modulus, yield strength, and thermal expansion. On the other hand, Denlinger et al. [24] assumed a reduction in the elastic modulus of the bulk material by a factor of 10^{-4}. These assumptions may influence the stability of the solution, since with the soft material consideration, consequently, deformations would be large.

1.4.4 Scale of the models

As highlighted before, modeling of the LPBF process consists of several challenges. Heat source models often require small time steps, temperature dependent material properties, high thermal gradients, powder phase consideration are some of the major ones. Consequently, it is often not possible to develop a complete part simulation which is involving detailed flow dynamics or microstructural properties due to the limited computational power. Hence, researchers often make certain assumptions based on their focus and either consider the domain micro, meso, or macro scales. Moreover, some multiscale models seek efficient approaches.

Qiu et al. [25] developed a Computational Fluid Dynamics (CFD) model using the C++ open-source CFD toolbox to investigate the effect of layer thickness and scan speed on porosity and surface structures in the LPBF process. They took into consideration of interfacial forces such as surface tension, Marangoni's flow, recoil pressure, drag, and buoyancy force in their model. Additional to these, the heat transfer occurs due to phase change, and evaporative heat losses were present in their model. As a requirement of a thermo-fluid model, conservation of momentum and energy, continuity, and volume-of-fluid were solved. A similar investigation was done by Zheng et al. [26] on the simulating melt pool and porosity formation in the LPBF process with a height function-lattice Boltzmann method (HF-LBM) coupled model. The lattice-Boltzmann method was preferred due to its computational efficiency on the mushy state melting/solidification interface problems. They used a mesh size of 2 μm as the resolution to accurately analyze powder particles. According to the author, their model was computationally efficient over the other approaches as Flow3D and ALE3D while using a GPU-based parallel computation.

Although detailed micro models give a good understanding of fluid dynamics in the melt pool, they are limited in terms of domain size because of the high computational work with the additional interfacial forces within the melt pool. Hence, to investigate the thermal and mechanical behavior of a region that is scanned with several hatches, and layers, a larger scale, and coarser resolution are needed.

Meso-scale models suit better for investigation of regions that are deposited by several hatches and layers. Resolution of meso-scale models is often limited by around 20-10 μm

minimum mesh size. Hence, in general, fluid dynamics within the melt pool are not considered. The continuum approach takes place for weakly coupled thermomechanical analysis so that mechanical deformation does not affect the thermal solution. The aim of these simulations is often to predict the thermomechanical behavior of a smaller region so that inference can be made for the process.

As it was mentioned before, due to moving heat source models that are commonly used in these models, a fine mesh should be applied to the heat-affected zone (HAZ). Non-uniform meshing is often preferred by the researchers, to ease the computational work and obeying the fine mesh requirement around HAZ at the same time. Denlinger et al. [24] developed a meso-scale computational model to investigate residual stress and distortion during the LPBF process. In their finite element model, they had used Goldak's double ellipsoid 3-D moving heat source to represent the laser heat source. To simulate deposition, powder elements were kept inactive until the deposition takes place in the particular layer. The phase change of powder to the solid properties was decided based on a criterion, where any of the quadrature points of an element should met with the heat source. Their finest mesh had dimensions of spot radius in longitudinal and transverse, and deposition thickness in the build direction. An adaptive dynamic meshing scheme was used with the software package Pan Computing® to decrease total element and node number, which allowed them to simulate 38 layers and a relatively large 91 mm^3 deposition volume. Luo et al. [27] also used a similar dynamic adaptive meshing strategy on their finite element thermal model that uses an open source finite element library, Deal II®, where mesh at the HAZ was refined during the simulation. The addition of a new powder layer was often simulated by activating the quiet elements within the mesh.

Boundary conditions (BCs) in meso-scale models are common as, convection and radiation at the top surface, conduction through powder and baseplate. Prescribed temperature or insulated surfaces at the bottom or sides can be used as well. Initial conditions are generally consisting a whole domain to a prescribed temperature to model pre-heating of the baseplate. Evaporation is neglected in most of the meso-scale approaches. For the mechanical BCs, only the bottom or bottom and side surfaces of the baseplate are constraints in displacement degree of freedom in most of the models [28].
Thermo-metallurgical-mechanical meso-scale models also focus on phase transformation phenomena additional to mentioned physics above. Tan et al. [29] proposed a finite

element model that considers solid-state phase transformation (SSPT) of two-phase titanium alloy Ti6Al4V for the prediction of residual stresses in ANSYS®. According to temperature history and cooling rates, the material undergoes solid-state transformations that alter the volume. Hence, volume shrinkage of the powder bed occurs after deposition and it was modeled by the again element birth/death method for multi-layers that is discussed in the latter paragraph. Additional consideration of volume strain due to SSPT ended up reducing the magnitude of the tensile stresses while increasing compressive stresses.

Rather than continuous moving heat source models, simplified heat inputs are also used. For the quick prediction of the temperature field Schwalbach et al. [30] developed a discrete source model to be used in PBF AM simulations with complex scan patterns. They had combined several stationary heat sources that were active at different time steps. Moreover, they assumed uniform thermal properties to avoid non-linearity for the analysis. The author state that for complex geometries and scan patterns, the discrete source model with these assumptions could ease the computational complexity. As discussed, each aspect of scaling in the modeling of LPBF has sort of assumptions and limitations. It is not possible to simulate part scale domains, with the considerations that are taken in micro and meso-scales due to computational work. Multi-scale modeling approaches aim to combine different scales to simulate macro-scale parts accurately. Li et. al. [31] studied multi-scale modeling to predict residual stresses and distortions in part-scale. They used a micro-scale model with a 3-D continuous moving heat source and gathered thermal field for a single track. It should be clarified that even though they called it “micro-scale” they did not account for any fluid dynamics within the melt pool. Next, they formulated an equivalent body force from the results of a micro-scale simulation. Lastly, this body force was applied to a cantilever beam that is on a macro-scale. According to their experimental results, they predicted distortion of the part with a maximum 28% error.

The inherent strain method (ISM) was first developed to increase the computational efficiency of welding simulations by Ueda et al. [32]. The total strain excluding thermal and elastic parts are called inherent strains. The maximum temperature and constraints at each direction are used to calculate inherent strains and they are put into elastic finite element analysis to find residual stresses and distortions. The methodology of ISM is

explained in detail in Chapter 6. Their methodology was later used in multiscale LPBF simulations to fast the prediction of RS and distortions in several articles [33],[34]. Bugatti et al. [35] found inherent strain tensors from a meso-scale simulation. Then, they conducted a simplified thermomechanical macro-scale simulation and with modified thermal expansion coefficients that were equal to inherent strains to find stresses and deformations. Additionality, calibration with experimental results was carried out and used for the improvement of ISM by the researchers. A similar methodology was also used by Chen et al. [36]. They used a fine scale model with 5 μm mesh size with a line heat input to extract related plastic strains. Moreover, certain modifications were made to make ISM more suitable for multi-layer AM processes.

1.5 Effect of process parameters in LPBF

As discussed before, one of the main aims of the modeling efforts is to understand and examine the influence of process parameters on the finished part. Porosity, surface quality, geometrical accuracy, and mechanical properties are some of the main concerns while selecting optimal parameters. Laser power and scan speed are the major parameters that directly affect the energy input. Energy input is proportional with laser power and inversely proportional with scan speed. Mukherjee et al. [37] stated that energy input had a direct correlation with thermal stain and volumetric shrinkage that would influence geometrical accuracy. Panda et al. [38] concluded the same behavior and also stated that an increase in laser power increased residual stresses and altering scan speed had the reverse effect on RS. A similar conclusion was made by Pohl et al. [39] that high energy input resulted in higher deformations and residual stresses thus author suggested using low laser power, high scan speed, large hatch distance, and layer thickness. Anderson et al. [40] also recommended increasing layer thickness to reduce stresses. By contrast to these findings, Mukherjee et al. [41] concluded that thinner layers would minimize the RS.

Isotropy of the mechanical properties, distortion rate, and distribution of stresses is also dependent on the scan strategy. In a single layer, Parry et al. [23] found that as the single scan vector length is increased stresses became larger. They also compared uniform and

zigzag scan patterns and even though both of them resulted in similar RS in magnitude-wise, the distribution of stresses varied depending on the scan pattern. During an investigation of the multi-layer effect, Robinson et al. [42] reported that the chequerboard scan strategy where a layer was divided into sub-regions and also alternation of scan direction didn't reduce RS significantly.

1.6 The objective of the study

As summarized in the latter section, conclusions were made by several studies on the influence of process parameters in LPBF process. However, different findings are present in terms of the effect of process parameters on residual stresses, hence literature still demands further research. The aim of this work was to develop an accurate meso-scale thermomechanical finite element model to predict thermal history, melt pool geometry, and residual stresses during the LPBF process. A method was proposed to account for surface heat losses including evaporation that can be used in other AM simulations as well. The model was developed as a parametric study so that influence process parameters such as laser power, scan speed, hatch spacing, and layer thickness on thermal and mechanical behavior were investigated. According to the results, certain arguments were made on the optimization of parameters. Moreover, a stress-based implementation of the inherent strain method was done to reduce computational time while predicting stresses with reasonable accuracy.

1.7 Thesis layout

In Chapter 2, temperature and phase dependent material properties are given. Next, in Chapter 3, the methodology is explained for the development of the thermomechanical model. In Chapter 4, an experimental study that was conducted to validate thermal simulation results is presented. In Chapter 5,the discussion is the parametric study that was done to determine the influence of process parameters and scan patterns on thermal and mechanical results. In Chapter 6, the original inherent strain theory is discussed, and the developed stress based method is described.

2 MATERIAL MODEL

In this study, Inconel® 718 (IN718 or alloy 718) powder was used as the processed material. The composition of it is shown in Table 2-1 [43]. It is a nickel-based superalloy mostly used in aerospace and defense industries because of its superior mechanical properties such as high yield strength. great creep and corrosion resistance. Due to its low machinability, it became popular to be used in AM methods. During the LPBF process temperatures within the material vary from ambient temperature, around 300 K, up to evaporation temperature which is around 3000 K depending on the process parameters. Hence, the thermal and mechanical properties of the material must be considered as temperature dependent to accurately model the material.

Table 2-1: Chemical composition of Inconel® 718 [43].

	%
Ni	50.00-55.00
Cr	17.00-21.00
Fe	Balance
Nb	4.75-5.50
Mo	2.80-3.30
Ti	0.65-1.15
Al	0.20-0.80
Co	1.00 max.
C	0.08 max.
Mn	0.35 max.
Si	0.35 max.
P	0.015 max.
B	0.006 max.
Cu	0.30 max

In Table 2-2 [44], thermal properties including density, ρ, specific heat, C_p and conductivity, k are shown for varying temperature range, and solid and liquid phases. Specific heat and conductivity were kept constant after the material is fully melted (above 1609 K). Emissivity values are shown in Table 2-3.

Table 2-2: Temperature dependent thermal properties of Inconel® 718 [44].

phase	T [K]	ρ [kg/m^3]	C_p [J/K/kg]	k [W/m/K]
solid	298	8190	435	8.9
solid	373	8160	455	10.8
solid	473	8118	479	12.9
solid	573	8079	497	15.2
solid	673	8040	515	17.4
solid	773	8001	527	18.7
solid	873	7962	558	20.8
solid	973	7925	568	21.9
solid	1073	7884	680	23.8
solid	1173	7845	640	25.8
solid	1273	7806	620	26.7
solid	1373	7767	640	28.3
solid	1443	7727	650	29.3
liquid	1609	7400	720	29.6
liquid	1673	7340	720	29.6
liquid	1773	7250	720	29.6
liquid	1873	7160	720	29.6

Table 2-3: Temperature dependent emissivity of Inconel® 718 [45].

T	[K]	543	558	757	873	882	1016	1067	1119	1281	1369
$\varepsilon^{(s)}$	[W/m^2/K]	0.23	0.24	0.26	0.28	0.28	0.3	0.31	0.31	0.32	0.33

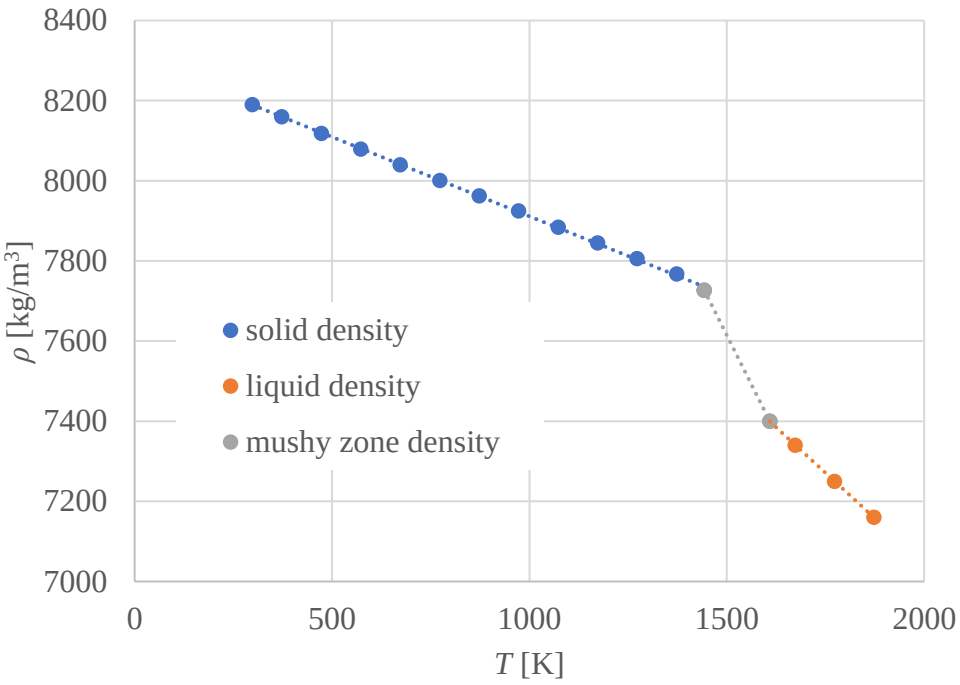

Figure 2-1: Linear fitting of temperature dependent density in different material phases.

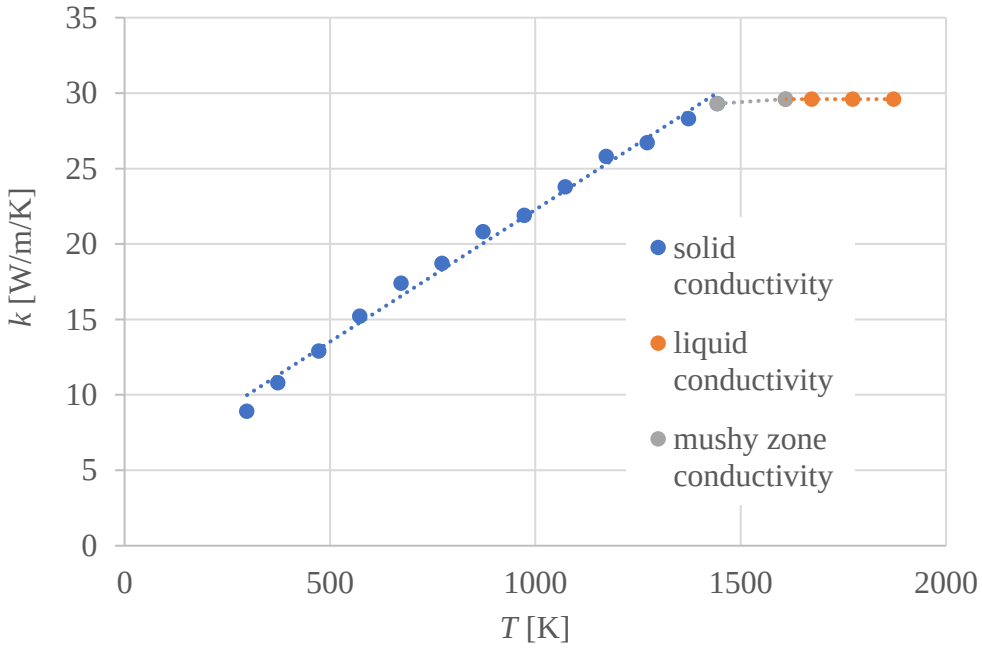

Figure 2-2: Linear fitting of temperature dependent conductivity in different material phases.

The conductivity of the liquid was enhanced by multiplying it with a factor of 2.5, to account for Marangoni convection, where the heat transfer rate is increased. For the implementation of the material properties into the developed computational model, material properties were linearly fitted as functions of temperatures as shown in Figure 2-1 and Figure 2-2. Moreover, for each phase; solid, liquid, and mushy zone, 3 different linear fit equations were used as shown in equation (2-1) for calculation of density. The solid fraction of the material during heating or cooling is determined by the values that are given in Table 2-4. The corresponding values were also linearly fitted as the function of temperature.

$$\rho = \begin{cases} 0.3961T + 8307, & 1440 < T \\ -1.9699T + 10570, & 1440 \leq T \leq 1609 \\ -0.9073T + 8859, & 1609 < T \end{cases} \quad (2\text{-}1)$$

Table 2-4: Solid fraction of the material according to temperature [44].

$f^{(s)}$	heating[K]	cooling[K]
0	1619	1608
0.1	1614	1605
0.2	1609	1601
0.3	1604	1597.5
0.4	1599	1593
0.5	1592	1588
0.6	1584	1583
0.7	1575	1573
0.8	1563	1564
0.9	1552	1550
1	1523	-

During the LPBF process, the powder is spread on a baseplate. The material of the plate is stainless steel 316 (SS316L). Most portion of the baseplate does not experience high temperature deviations as the deposited material does, hence constant material properties are used as shown in Table 2-5.

Table 2-5: Properties of stainless steel 316l [46].

ρ	C_p	k_s	α	E	Y	v
[kg/m^3]	[J/K/kg]	[W/m/K]	[K^{-5}]	[GPa]	[MPa]	-
7700	481	14	1.17	198.5	282	0.3

2.1 Powder properties

During the LPBF process, material experiences three phases that are solid, liquid, and powder. The solid and liquid properties were formulated as functions of temperature as explained in the latter section. The state of the material phase was determined by the temperature. Modeling of the powder bed properties was very crucial since it affects the heat transfer mechanism in the thermal model and the stability of the mechanical model. The conductivity of the material reduces drastically in the powder phase because of the high porosity. This reduction prevents heat dissipation, and heat energy becomes localized, and consequently, temperature gradients become larger.

$$\omega = \begin{cases} -1, & powder \\ 0, & solid \\ 1, & liquid \end{cases} \tag{2-2}$$

Powder bed conductivity was calculated by the equation (2-3) below [47], in terms of porosity, φ, a constant, f_0, scaling factor, a, and conductivity of the surrounding argon gas, $k^{(Ar)}$. ζ is the ratio of conductivity of solid $k^{(s)}$ over conductivity of Argon gas as shown in equation (2-3-3). Calibration constant, f_0, scaling factor, a calculated with using porosity. Porosity was used as 0.3 in this study, while conductivity of Argon gas was taken as 0.016 W/m/K [24].

$$\frac{k^{(p)}}{k^{(Ar)}} = (1-a)\frac{\varphi f_0 + \zeta(1-\varphi f_o)}{1-\varphi(1-f_0)+\kappa\varphi(1-f_0)} + a\frac{2\zeta^2(1-\varphi)+(1+2\varphi)\zeta}{(2+\varphi)\zeta+1-\varphi} \tag{2-3}$$

$$f_0 = 0.8 + 0.1\varphi \tag{2-3-1}$$

$$\log(a) = \begin{cases} -4.898\varphi, & 0 \le \varphi < 0.0827 \\ -0.405 - 3.154(\varphi - 0.0827), & 0.0827 \le \varphi < 0.298 \\ -1.084 - 6.778(\varphi - 0.298), & 0.298 \le \varphi < 0.580 \end{cases} \tag{2-3-2}$$

$$\zeta = \frac{k^{(s)}}{k^{(Ar)}} \tag{2-3-3}$$

Density and specific heat of the powder phase were calculated by using porosity and its solid properties as shown below in equations (2-4) and (2-5) respectively.

$$\rho^{(p)} = (1 - \varphi)\rho^{(s)} \tag{2-4}$$

$$C_p^{(p)} = (1 - \varphi)C_p^{(s)} \tag{2-5}$$

The equation (2-6) below shows the relation of emissivity of the powder phase with the solid phase, $\varepsilon^{(s)}$. The porous area fraction, $A^{(H)}$, and emissivity of the powder surface vacancies, $\varepsilon^{(H)}$ are calculated by using equations (2-6-1) and (2-6-2) respectively [21].

$$\varepsilon^{(p)} = A^{(H)}\varepsilon^{(H)} + (1 - A^{H})\varepsilon^{(s)} \tag{2-6}$$

$$A^{(H)} = \frac{0.908\varphi}{1.908\varphi - \varphi^2 + 1} \tag{2-6-1}$$

$$\varepsilon^{(H)} = \frac{\varepsilon^{(s)}[2 + 3.082\left(\frac{1-\varphi}{\varphi}\right)^2]}{\varepsilon^{s}\left[1 + 3.082\left(\frac{1-\varphi}{\varphi}\right)^2\right] + 1} \qquad (2\text{-}6\text{-}2)$$

Table 2-6 shows temperature dependent modulus of elasticity, *E*, yield strength, *Y*, poisons ratio, ν, and thermal expansion coefficient, α. The properties were linearly fitted as functions of temperature as it was done for thermal properties. For the temperatures above the melting point (1609 K) modulus of elasticity and yield strength were assumed as constant and equal to 1 GPa and 1 MPa respectively. Modulus of elasticity and yield stress of powder were calculated by reducing solid-phase properties by a factor of 10^{-3}. Although for liquid and powder states these values may still be large, however, since within the process high deformations and stresses occur, the values were selected considering also the stability of the model.

Table 2-6: Temperature dependent mechanical properties of Inconel® 718 [24], [43].

T [K]	*E* [Pa]	*Y* [Pa]	ν -	α [1/K]
294	$2.08\text{x}10^{11}$	$1.17\text{x}10^{9}$	0.25	$1.17\text{x}10^{-5}$
366	$2.05\text{x}10^{11}$	$1.17\text{x}10^{9}$	0.31	$1.28\text{x}10^{-5}$
477	$2.02\text{x}10^{11}$	$1.12\text{x}10^{9}$	0.31	$1.34\text{x}10^{-5}$
589	$1.94\text{x}10^{11}$	$1.10\text{x}10^{9}$	0.27	$1.46\text{x}10^{-5}$
700	$1.86\text{x}10^{11}$	$1.08\text{x}10^{9}$	0.27	$1.51\text{x}10^{-5}$
811	$1.79\text{x}10^{11}$	$1.07\text{x}10^{9}$	0.27	$1.57\text{x}10^{-5}$
922	$1.72\text{x}10^{11}$	$1.03\text{x}10^{9}$	0.28	$1.66\text{x}10^{-5}$
1033	$1.62\text{x}10^{11}$	$7.58\ \text{x}10^{8}$	0.31	$1.66\text{x}10^{-5}$
1144	$1.27\text{x}10^{11}$	-	0.33	$1.42\text{x}10^{-5}$
1227	$7.80\text{x}10^{11}$	-	0.34	$1.08\text{x}10^{-5}$
1609	$1.00\ \text{x}10^{9}$*	$1.00\text{x}10^{6}$*	0.34	$7.48\text{x}10^{-5}$

$$E^{(p)} = E\text{x}10^{-3} \tag{2-7}$$

$$Y^{(p)} = Y\text{x}10^{-3} \tag{2-8}$$

2.2 Summary

In this chapter, considerations for material modeling efforts are presented. Temperature dependent thermal and mechanical properties were used for the deposition material (Inconel 718®). Moreover, for each phase (powder, liquid and, solid) additional considerations were made by using related equations from the literature. Temperature dependent properties were linearly fitted to be used in the developed finite element model. On the other hand, constant parameters were used to represent the base plate material since temperature variations were not dramatic as the deposited material.

3 THERMOMECHANICAL LASER POWDER BED FUSION PROCESS MODEL

In this chapter, thermomechanical LPBF process model is explained. In the beginning, governing equations for thermal and mechanical models are presented. Then discretization of these for the application of finite element analysis is described. Next, procedures for mesh and scan path generation and the decision of the element size are explained in detail.

3.1 Thermal model

The strong form of the transient heat transfer derived from the energy balance equation is given in (3-1) below. In equation (3-1), ρ is the mass density and C_p is the specific heat of the material. **q** is the heat flux vector as a function of time, *t*, and position, **x**. Heat input is given by $\dot{Q}$, and $\dot{q}_{loss}$ is the heat losses from the system that accounts for convection, radiation, and evaporation losses through the surface as shown by equation (3-4).

$$\rho C_p \frac{\partial T}{\partial t} = -\boldsymbol{\nabla}.\mathbf{q}(\mathbf{x},t) + \dot{Q}(\mathbf{x},t) - \dot{q}_{loss} \tag{3-1}$$

The heat flux vector was gathered from thermal gradients in three-dimensional space as shown in equation (3-2).

$$\mathbf{q}(\mathbf{x},t) = -\mathbf{k}\boldsymbol{\nabla}T = -\mathbf{k}\left(\frac{\partial^2 T}{\partial x^2} + \frac{\partial^2 T}{\partial y^2} + \frac{\partial^2 T}{\partial z^2}\right) \tag{3-2}$$

Isotropic conductivity was used in normal directions (x, y, z) as shown below.

$$\mathbf{k} = \begin{bmatrix} k & 0 & 0 \\ 0 & k & 0 \\ 0 & 0 & k \end{bmatrix} \tag{3-3}$$

$$\dot{q}_{loss}(\mathbf{x_s}, t) = \dot{q}_{conv} + \dot{q}_{rad} + \dot{q}_{evap} \quad (3\text{-}4)$$

The convective heat transfer loss from the surface was defined as equation (3-5) where h is the convective heat transfer coefficient and T_0 is the ambient temperature. It is a function of time, t, and position on the surface $\mathbf{x_s}$.

$$\dot{q}_{conv}(\mathbf{x_s}, t) = h(T - T_0) \quad (3\text{-}5)$$

The radiative heat loss was gathered from equation (3-6). ε and K_B stand for emissivity and Boltzmann constant respectively.

$$\dot{q}_{rad}(\mathbf{x_s}, t) = \varepsilon K_B(T^4 - T_0^4) \quad (3\text{-}6)$$

Evaporative heat losses were computed from equation (3-7) shown below, where T_s and T_v are surface and boiling temperatures respectively [48]. ΔH_v^* and M are effective enthalpy and molar mass of the metal vapor. R is the universal gas constant. The constants that were used are given in Table 3-1.

$$\dot{q}_{evap}(\mathbf{x_s}, t) = \frac{0.82\Delta H_v^*}{\sqrt{2\pi M R T_s}} P_0 \exp\left(\frac{\Delta H_v^*(T_s - T_v)}{R T_s T_v}\right) \quad (3\text{-}7)$$

Table 3-1: Constants for surface heat losses [49]

h [W/m^{2}K]	K_B [J/K]	M [g/mol]	R [J/mol/K]	ΔH_v^* [J/g]	T_v [K]
25	1.381×10^{-23}	59.75	8.314	6.4×10^3	3188

3.1.1 Volumetric Heat Source Model

To model the laser beam heat source, the volumetric semi-ellipsoid heat source model that was proposed by Goldak was used as shown in equation (3-8) [50]. In this equation, P is the laser power, η is the efficiency factor. x', y', and z' are relative distances with respect to center of the laser beam. r_x and r_y are radii of the laser beam and r_z is the penetration depth, that are given in Table 3-2.

$$\dot{Q}(\mathbf{x},t)=\frac{6\eta\sqrt{3}P}{\pi\sqrt{\pi}r_x r_y r_z}\exp\left(-\frac{3x'^2}{r_x^2}\right)\exp\left(-\frac{3y'^2}{r_y^2}\right)\exp\left(-\frac{3z'^2}{r_z^2}\right) \tag{3-8}$$

Table 3-2: Laser beam constants.

r_x, r_y [μm]	r_z [μm]	η -
50	150	0.3

The lumped efficiency term, η, was selected as 0.3 for the solid material but a larger value that is 0.66 was used for the powder, to account for the increase in absorptivity.

3.2 Mechanical model

In the mechanical model, an elastic-perfectly plastic material model was used. Linear momentum balance is given by equation (3-9), where **v** is the velocity vector. Left-hand side (LHS) of the equation states that the linear momentum is conserved over time and it is equal to the **F,** which indicates the total force acting on a body [51].

$$\frac{\mathrm{d}}{\mathrm{dt}}\left[\iiint \rho\mathbf{v}\right]\mathrm{dV}=\mathbf{F} \tag{3-9}$$

The total force consists of body force **b**, and traction **t**, as shown in equation (3-10).

$$\mathbf{F}=\iiint \rho\mathbf{b}\,\mathrm{dV}+\iint \mathbf{t}\,\mathrm{dA} \tag{3-10}$$

Traction is expressed as projections of stress tensor on an area normal, **n**, and it is put into equation (3-10).

$$\mathbf{t}=\boldsymbol{\sigma}.\mathbf{n} \tag{3-11}$$

$$\mathbf{F}=\iiint \rho\mathbf{b}\,\mathrm{dV}+\iint \boldsymbol{\sigma}.\mathbf{n}\,\mathrm{dA} \tag{3-12}$$

Area integral can be expressed as volume integral by using Gauss's theorem.

$$\iint \boldsymbol{\sigma}.\mathbf{n}\,\mathrm{dA}=\iiint \boldsymbol{\nabla}.\boldsymbol{\sigma}\,\mathrm{dV} \tag{3-13}$$

The final form of the weak form of the linear momentum balance is shown in equation (3-14).

$$\iiint \rho \mathbf{a} \mathrm{dV} = \iiint \rho \mathbf{b} \mathrm{dV} + \iiint \boldsymbol{\nabla}.\boldsymbol{\sigma} \mathrm{dV} \tag{3-14}$$

The integrals can be eliminated since they are all volumetric. If there is no body force or acceleration, static equilibrium can be achieved as shown in equation (3-16).

$$\rho \mathbf{a} = \rho \mathbf{b} + \boldsymbol{\nabla}.\boldsymbol{\sigma} \tag{3-15}$$

$$\boldsymbol{\nabla}.\boldsymbol{\sigma} = 0 \tag{3-16}$$

Total strain consists of plastic, elastic, and thermal parts as shown in equation (3-17).

$$\boldsymbol{\epsilon} = \boldsymbol{\epsilon_{plastic}} + \boldsymbol{\epsilon_{elastic}} + \boldsymbol{\epsilon_{thermal}} \tag{3-17}$$

Thermal strain is described with thermal expansion coefficient multiplied by temperature difference from the initial, steady-state condition.

$$\boldsymbol{\epsilon_{thermal}} = \alpha \Delta T \tag{3-18}$$

Stress tensor is gathered by double contraction of elastic strains tensor with elasticity matrix, $\mathbf{C}$.

$$\boldsymbol{\sigma} = \mathbf{C} : \boldsymbol{\epsilon_{elastic}} \tag{3-19}$$

$$\mathbf{C} = \frac{E}{(1+\nu)(1-2\nu)} \begin{bmatrix} 1-\nu & \nu & \nu & 0 & 0 & 0 \\ \nu & 1-\nu & \nu & 0 & 0 & 0 \\ \nu & \nu & 1-\nu & 0 & 0 & 0 \\ 0 & 0 & 0 & 1-2\nu & 0 & 0 \\ 0 & 0 & 0 & 0 & 1-2\nu & 0 \\ 0 & 0 & 0 & 0 & 0 & 1-2\nu \end{bmatrix} \tag{3-20}$$

Deviatoric stress tensor, $\boldsymbol{\sigma}'$, is found by subtracting mean stress from the stress.

$$\boldsymbol{\sigma}' = \boldsymbol{\sigma} - \frac{\mathbf{I}}{\mathbf{3}} \mathrm{tr}(\boldsymbol{\sigma}) \tag{3-21}$$

The scalar measure of stress, that is Von-Mises stress is described with deviatoric stress in equation (3-22) to be used as the criteria of yielding.

$$\sigma_{VM} = \sqrt{\frac{3}{2}\boldsymbol{\sigma}' : \boldsymbol{\sigma}'} \tag{3-22}$$

Plastic strain increment can be expressed as in equation (3-23), where $\mathbf{n_p}$ is to determine direction of the flow and Δp for the magnitude. $\mathbf{n_p}$ can be computed with deviatoric stress and Von-Mises stress.

$$\Delta \boldsymbol{\epsilon_{plastic}} = \mathbf{n_p} \Delta p \tag{3-23}$$

$$\mathbf{n_p} = \frac{3}{2}\left(\frac{\boldsymbol{\sigma}'}{\sigma_{VM}}\right) \tag{3-24}$$

The Von Mises function is given in equation (3-25). The yield function uses deviatoric stresses, hence hydrostatic stress does not affect yielding. As long as function ψ was smaller than zero there will be no plastic deformation occur. Otherwise, the plastic strain rate was computed by solving iteratively at each time increment [51].

$$\psi(\boldsymbol{\sigma}, \Delta p) = \sigma_{VM} - Y(\Delta p, T) = \sqrt{\frac{3}{2}\boldsymbol{\sigma}' : \boldsymbol{\sigma}'} - Y(\Delta p, T) \tag{3-25}$$

3.3 Finite element method

The finite element method (FEM) is a numerical method that allows approximating analytically unsolvable or difficult problems by discretizing the partial differential equations. Since it can give approximate solutions with reasonable accuracy, it is one of the most popular numerical methods. A domain is discretized with elements with finite and known geometries and elements are connected via nodes as shown in Figure 3-1.

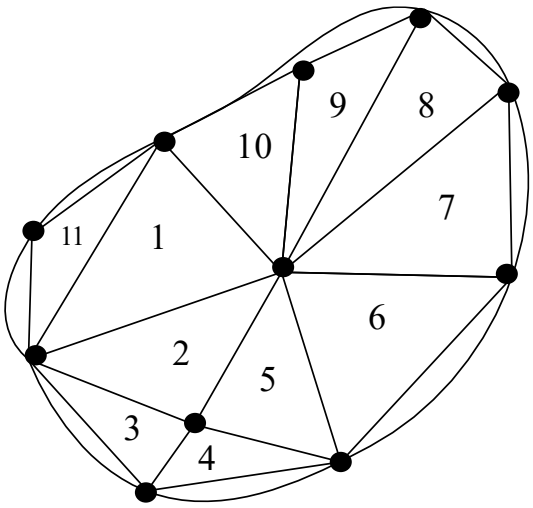

Figure 3-1: Example of discretization of a body

Interpolation or shape functions are used for mapping the solution over the discretized domain to compute values at the nodes. The interpolation of temperature over an element is obtained by equation (3-26). $\mathbf{N}(\mathbf{x})$ is the interpolation function of a finite element. Temperatures at the nodes, $\widehat{\mathbf{T}}$, can be computed.

$$T(\mathbf{x}) = \mathbf{N}(\mathbf{x})\widehat{\mathbf{T}} \tag{3-26}$$

The transient energy balance can be expressed in the weak form to be discretized for FEM application as described in equation (3-27). $\mathbf{C_P}$ is the heat capacitance matrix, $\mathbf{K}$ is the global conductivity matrix and $\mathbf{Q}$ is the heat load vector. $\mathbf{T}_\mathbf{t}$ is the temperature at the nodes for the former time increment and with a time increment of Δt, equation can be solved for temperature at the nodes for the next time increment $\widehat{\mathbf{T}}$ [52].

$$[\mathbf{K}]\widehat{\mathbf{T}} + [\mathbf{C_P}]\left(\frac{\widehat{\mathbf{T}} - \widehat{\mathbf{T}}_\mathbf{t}}{\Delta t}\right) = \{\mathbf{Q}\} \tag{3-27}$$

The heat capacitance matrix is computed using the interpolation functions as shown in the equation below.

$$[\mathbf{C_P}] = \iiint \mathbf{N}^\mathrm{T}\boldsymbol{\rho C_p}\mathbf{N}dV \tag{3-28}$$

Similarly, the conductivity matrix is gathered using the gradient of interpolation functions, as shown in equation (3-29).

$$[\mathbf{K}] = \iiint \nabla \mathbf{N}^{\mathrm{T}} \mathbf{k} \nabla \mathbf{N} dV \tag{3-29}$$

The heat load vector consists of volumetric heat input and surface heat loss terms. **n** is the surface normal that heat loss occurs.

$$\{\mathbf{Q}\} = \iiint \mathbf{N}^{\boldsymbol{T}} \dot{Q} dV - \iint \mathbf{N}_{\boldsymbol{s}}^{\mathrm{T}} \mathbf{q}_{\mathbf{loss}} . \mathbf{n} \mathrm{d}S \tag{3-30}$$

For the mechanical model discretization of displacements, $\mathbf{u}(\mathbf{x})$, are done as shown in the equation using interpolation functions. Hence, the nodal displacements, $\hat{\mathbf{u}}$, can be mapped as follows:

$$\mathbf{u}(\mathbf{x}) = \mathbf{N}(\mathbf{x})\hat{\mathbf{u}} \tag{3-31}$$

The displacements are related to the strains using the strain-displacement coupling, **B**, as shown in equation (3-32). **B** is the gradient of the interpolation functions.

$$\boldsymbol{\epsilon} = \mathbf{B}\hat{\mathbf{u}} \tag{3-32}$$

Finally, equation (3-16), which is static mechanical equilibrium under no body forces, is discretized to be used in FEM application, as described in (3-33).

$$\iiint \mathbf{B}^{\mathrm{T}} \boldsymbol{\sigma} dV = 0 \tag{3-33}$$

3.3.1 Gauss quadrature numerical integration

The shown integrals are solved via numerical integration during finite element analysis. There are numerical methods such as the trapezoid rule and Simpson's formula, but the most widely used technique in finite element analysis is the Gauss quadrature.

To demonstrate an example, the volumetric integral of a function *f*, over a 2x2x2 cube is given in equation (3-34). The 3-dimensional space is given in directions of r, s, and t.

$$I = \int_{-1}^{1} \int_{-1}^{1} \int_{-1}^{1} f(r, s, t) dr ds dt \tag{3-34}$$

In equation (3-35), the numerical integration procedure is shown. m, n, and p are the number of quadrature points in directions r, s, and t respectively. The *w* term is the weight of the functions depending on the Gauss point locations [53].

$$I \approx \sum_{i=1}^{m}\sum_{j=1}^{n}\sum_{k=1}^{p} w_i w_j w_k f(r_i, s_j, t_k) \tag{3-35}$$

Table 3-3 shows the coordinates of Gauss quadrature points for an 8 node cubic element with an edge length of 2 units. The Gaussian points are located with a distance of 0.57735 $(1/\sqrt{3})$ to the center in each direction. There are 8 Gauss quadrature points and the weight (w) value is 1 for the whole.

Table 3-3: Coordinates of quadrature points for a 2x2x2 cube [53].

Points	r_i	s_j	t_k
1	-0.57735	-0.57735	-0.57735
2	-0.57735	-0.57735	-0.57735
3	-0.57735	0.57735	-0.57735
4	-0.57735	0.57735	0.57735
5	0.57735	-0.57735	-0.57735
6	0.57735	-0.57735	0.57735
7	0.57735	0.57735	-0.57735
8	0.57735	0.57735	0.57735

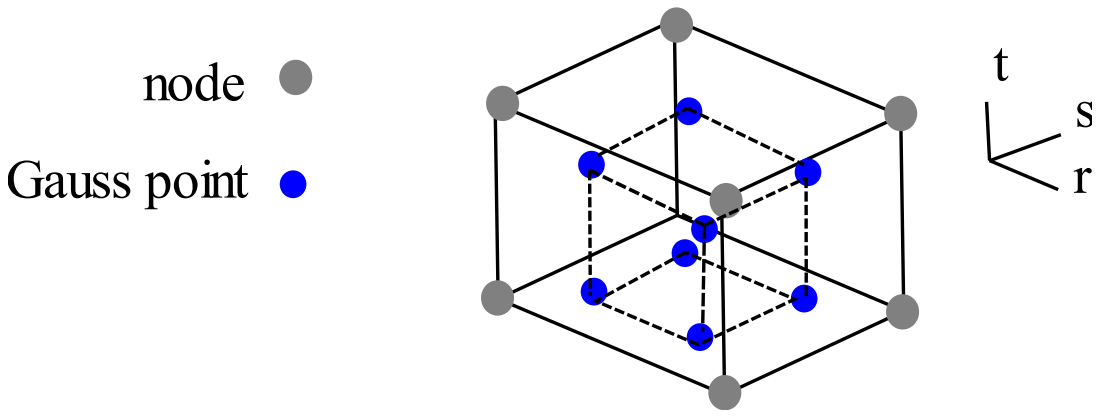

Figure 3-2: A volume finite element with 8 Gauss points

Figure 3-2 describes a 3-dimensional element with 8 nodes and Gauss points. In terms of Gauss points and dimensions, a 2x2x2 cube is given as an example. In this study hexahedral (HEX8) elements were used, which is similar to the cube example that is given but edge length can have different values in every three directions.

3.3.2 The solution of non-linear problems

Since temperature dependent material properties were considered in the model as presented in Chapter 2, the problem became non-linear. Newton-Raphson method was being used during the solution procedure by the commercial finite element solver MSC MARC®. In this method, the solution is gathered with first assuming one and then improved over the iterations.

In equation (3-36), $\boldsymbol{\kappa}$, is the internal force vector, that is a function of an unknown set of displacement vector $\mathbf{u}$, and it should be equal to the $\mathbf{R}_{\mathrm{E}}$ which is the external load vector.

$$\boldsymbol{\kappa}(\mathbf{u}) = \mathbf{R}_{\mathrm{E}} \tag{3-36}$$

The global internal force vector is computed using the mechanical equilibrium that is presented in equation (3-37).

$$\boldsymbol{\kappa}(\mathbf{u}) = \sum_{el} \iiint \mathbf{B}^{\mathrm{T}} \boldsymbol{\sigma} \mathrm{dV} \tag{3-37}$$

As shown in equation (3-38), the solution is assumed in i$^{\mathrm{th}}$ increment as $\mathbf{u}^{\mathbf{i}}$. Superscript 'i' indicates the solution increment step. $\Delta\mathbf{u}^{\mathbf{i}}$ is the increment of the solution, and $\boldsymbol{\kappa}_{\boldsymbol{T}}^{\boldsymbol{i}}$ is the tangent stiffness matrix that is shown in equation (3-39).

$$\boldsymbol{\kappa}\left(\mathbf{u}^{\mathrm{i+1}}\right) \approx \boldsymbol{\kappa}(\mathbf{u}^{\mathbf{i}}) + \boldsymbol{\kappa}_{\boldsymbol{T}}^{\boldsymbol{i}} \Delta\mathbf{u}^{\mathbf{i}} = \boldsymbol{R}_{E} \tag{3-38}$$

$$\boldsymbol{\kappa}_{t}^{i} = \begin{pmatrix} \frac{\partial \kappa_1(\mathbf{u}^i)}{\partial u_1} & \frac{\partial \kappa_1(\mathbf{u}^i)}{\partial u_2} & \cdots & \frac{\partial \kappa_1(\mathbf{u}^i)}{\partial u_n} \\ \frac{\partial \kappa_2(\mathbf{u}^i)}{\partial u_1} & \frac{\partial \kappa_2(\mathbf{u}^i)}{\partial u_2} & \cdots & \frac{\partial \kappa_2(\mathbf{u}^i)}{\partial u_n} \\ \vdots & \vdots & \ddots & \vdots \\ \frac{\partial \kappa_n(\mathbf{u}^i)}{\partial u_1} & \frac{\partial \kappa_n(\mathbf{u}^i)}{\partial u_2} & \cdots & \frac{\partial \kappa_n(\mathbf{u}^i)}{\partial u_n} \end{pmatrix}, \qquad \Delta\mathbf{u}^{\mathbf{i}} = \begin{bmatrix} \Delta u_1 \\ \Delta u_2 \\ \vdots \\ \Delta u_n \end{bmatrix} \tag{3-39}$$

The simplified version of equation (3-38) is shown below. $\Delta\mathbf{u^i}$ can be solved with the assumed solution.

$$\boldsymbol{\kappa}_{\boldsymbol{T}}^{i}\Delta\mathbf{u}^{i} = \boldsymbol{R}_{E} - \boldsymbol{\kappa}(\mathbf{u}^{i}) \tag{3-40}$$

After calculating $\Delta\mathbf{u^i}$, with an assumed solution, the next increment's solution can be calculated as follows:

$$\mathbf{u}^{i+1} = \mathbf{u}^{i} + \Delta\mathbf{u} \tag{3-41}$$

The residual force in the non-linear solution is computed as shown below [53].

$$\boldsymbol{R}^{i+1} = \boldsymbol{R}_{E} - \boldsymbol{\kappa}(\mathbf{u}^{i+1}) \tag{3-42}$$

Based on the convergence criteria the calculated residual can be assumed as the solution. The convergence criteria that was used in this study was 0.1.

$$\text{convergence} = \frac{\|\mathbf{R}^{i+1}\|^2}{1 + \|\mathbf{R}_E\|^2} \tag{3-43}$$

Apart from the mechanical solution, convergence for the thermal solution was ensured by limiting the temperature update at each iteration to a tolerance value, which was set as 100 K for the current study.

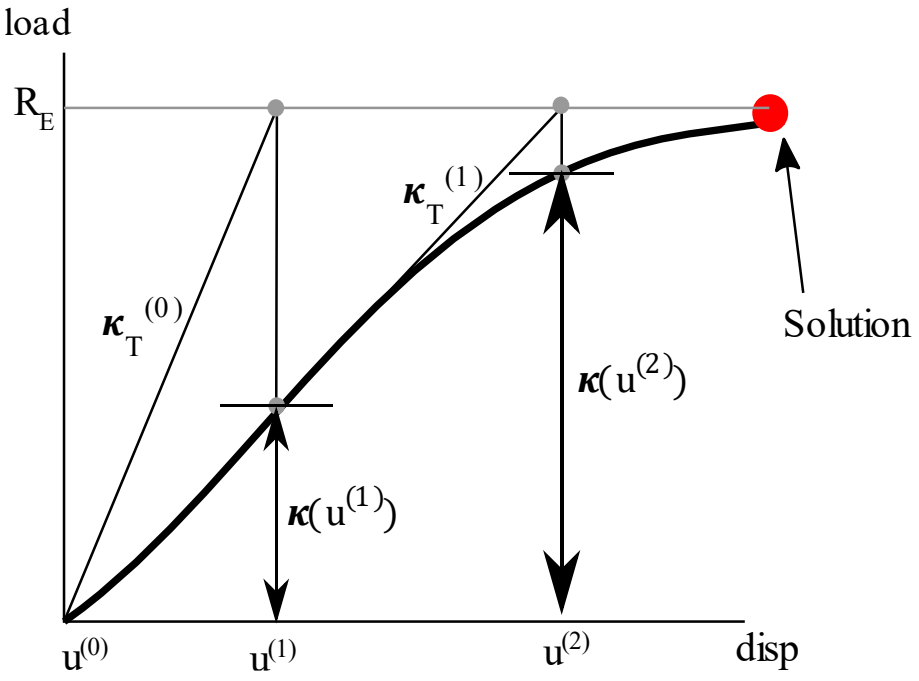

Figure 3-3 Schematic for Newton-Raphson iteration [53].

Figure 3-3 shows the discussed iteration methodology of the Newton-Raphson method schematically. At each iteration, tangent stiffness is formed again and the assumed solution for displacements is updated until the difference between residual and reaction forces is within the tolerance.

3.4 Gauss's theorem

Most of the commercial finite element software requires surface heat fluxes to be determined on the free surfaces. However, in AM models layer-by-layer manufacturing is often simulated by activating the upcoming layers on top of the deposited material. Hence, it is required to define free surfaces again and again for each layer.

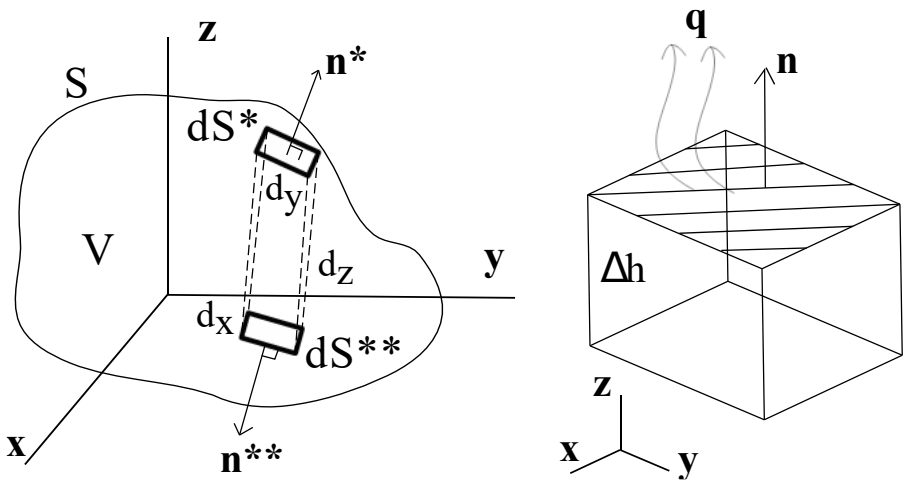

Figure 3-4: Two arbitrary surfaces and their normal (left), a finite element and surface flux from the top (right) [54].

In Figure 3-4 a schematic is given to support the description of Gauss's (or divergence) theorem and its application to the model in the present study. Suppose A is an arbitrary function over the surface S as shown in Figure 3-4 on the left-hand side. Then the equation (3-44) can be formulated, where A^* and A^{**} are the values of A on the top and bottom surfaces along the x-axis. The change of function A along x over the volume can be represented via surface values at two ends.

$$\iiint \frac{\partial A}{\partial x} dV = \iint (A^* - A^{**}) \mathrm{d}S \tag{3-44}$$

The right-hand side of equation (3-44) can be written as in equation (3-45) via the surface normal of top and bottom ends along the x-direction, $\mathbf{n}^*$ and $\mathbf{n}^{**}$. Note that minus sign is vanished since bottom surface normal, $\mathbf{n}^{**}$, has the minus sign also. Then the expression can be simplified with $\mathbf{n}$, that is unit normal of surface S along x. Finally, the whole term can be represented as the divergence of function *A* over the volume [54].

$$\iint (A^*.\mathbf{n}^* + A^{**}.\mathbf{n}^{**})\mathrm{d}S = \iint A.\mathbf{n}\mathrm{d}S = \iiint \nabla.A\mathrm{d}V \tag{3-45}$$

Similarly, for the right-hand side of Figure 3-4, surface heat loss vector, $\mathbf{q}_{loss}$, can be written as the divergence of it over the volume as shown below:

$$\iint \mathbf{q}_{loss}.\mathbf{n}\mathrm{d}S = \iiint \nabla.\mathbf{q}_{loss}\mathrm{d}V \tag{3-46}$$

Since it was assumed that only surface heat loss occurs along build direction (z-direction), divergence term was written as the magnitude of surface losses over the thickness of layer, Δh. Hence, the surface heat losses were directly given as a negative volumetric heat input. This is a very practical methodology for most AM simulations.

$$\nabla.\mathbf{q}_{loss} = \frac{\partial q_{loss}}{\partial x} + \frac{\partial q_{loss}}{\partial y} + \frac{\partial q_{loss}}{\partial z}, \qquad \frac{\partial q_{loss}}{\partial x} + \frac{\partial q_{loss}}{\partial y} = 0, \quad \frac{\partial q_{loss}}{\partial z} = \frac{q_{loss}}{\Delta h} \tag{3-47}$$

3.5 Simulation algorithm

The FE model was developed on the commercial finite element software MSC MARC® together with user-defined subroutines that were written in the FORTRAN® language. All constants and inputs that were necessary for the simulation were given in MATLAB® codes. The MATLAB® codes consisted of constants to calculate temperature dependent properties, and also inputs related to process parameters such as the number of layers, laser power, scan speed, hatch space, layer thickness, and beam radius. Moreover, finite element inputs such as dimensions of the hatched area and baseplate, and also the meshing scheme was defined in these files as inputs. Then, a procedure file was formed from these MATLAB® files which was read by the MSC MARC® to generate the model and store

the necessary input constants. There were several advantages of using these MATLAB® files at the beginning. Firstly, this allowed running a parametric study, since all the input parameters can be altered very easily and systematically. Additionally, generating the model manually rather than using a procedure file was very time consuming due to the complexity of the model generation procedure.

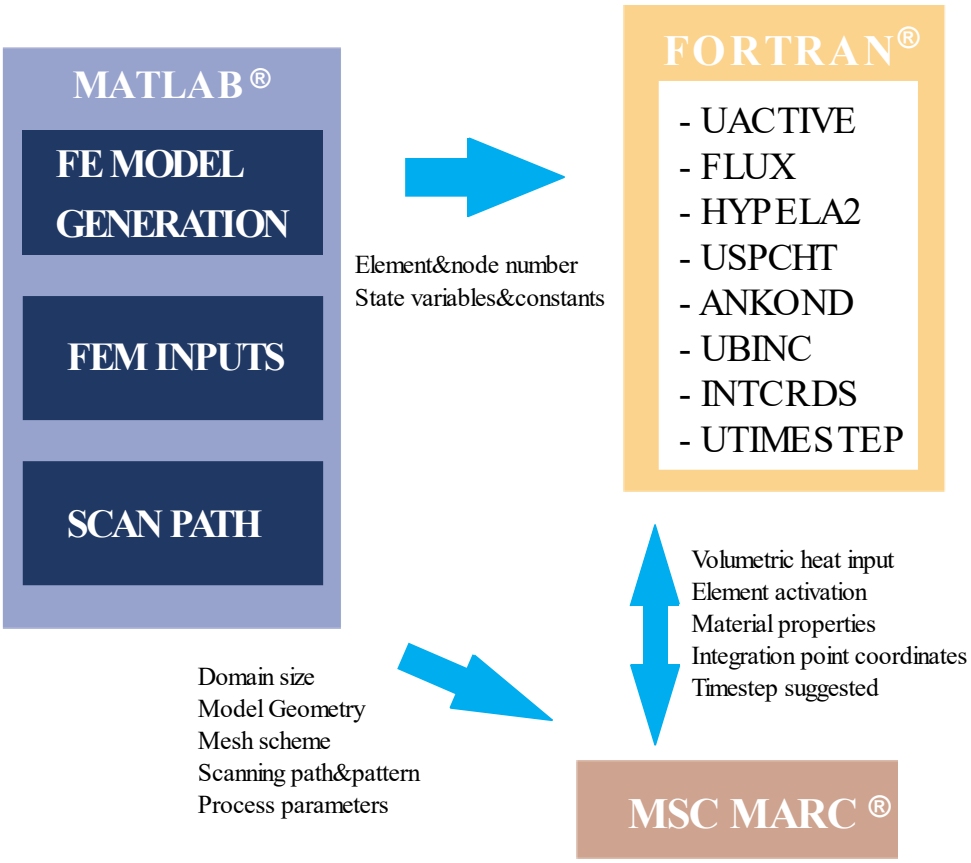

Figure 3-5: Block diagram for the model generation and FE analysis.

The relationship between MATLAB® input files, user-defined subroutines, and MSC MARC® is given in Figure 3-5. As explained, first, MATLAB® files form a procedure file to generate the mesh and model in the MSC MARC®. Then, while the simulation is running several user-defined FORTRAN® sub-routines are used. Calculations such as those to determine the temperature dependent material properties, the desired time step, and the phase determination of the material for each time step were performed using these subroutines. MSC MARC® uses all the calculated values to solve the thermomechanical finite element analysis with the numerical methods that described previously and also

presented results by creating a result file based on the solution. A description of the subroutines that are used is given below.

- UBINC: This subroutine was used to initializing and updating all the state variables at the beginning of an increment.

- UTIMESTEP: This subroutine was to adjust the time step for each increment. Although software automatically chooses the time step that was required based on the thermal and mechanical convergence criteria, the user still can suggest any time step. The algorithm for time intervals and steps that were used is discussed in the further section.

- UACTIVE: Since manufacturing in the LPBF process is done layer-by-layer, active/deactive element method was used in this study. Mesh was generated for the whole part but layers were kept deactivate until the corresponding layer was being deposited. This is called layer-by-layer activation.

- INTCRDS: The subroutine was used to gather coordinates of integration (or Gauss quadrature) points of every element.

- USPCHT: This subroutine was used to compute specific heat as a function of temperature by using the constant and linear equations from the MATLAB® files. Also based on the state of the material (powder, liquid or solid) the necessary modification was done.

- ANKOND: This subroutine was used to temperature dependent conductivity of the material. Moreover, powder conductivity was calculated separately by using equation (2-3).

- FLUX: In this subroutine, the amount of total volumetric heat flux was calculated and given into integration points by using equation (3-8). The surface losses were also given as a negative volumetric heat source as given in equation (3-47). For each increment, the position of the moving heat source was updated.

- HYPELA2: The sub-routine was used to define the material behavior of the material for the mechanical solution. The decision for the yield and elastic-perfectly plastic material definition was done in this routine and elastic and plastic strains were distinguished and stresses were found based on the temperature dependent mechanical properties. This subroutine also allowed to define different mechanical properties for each phase such as powder, liquid, or solid.

3.6 Mesh scheme and boundary conditions

The FE mesh and boundary conditions (BCs) were shown in Figure 3-6. Thermal BCs consist; moving heat source as the input and surface heat losses that were radiation convection and evaporation. All of them were given as volumetric input as discussed before. The ambient temperature was assumed to be 298 K. The bottom surface of the baseplate was fixed at the preheated temperature that was 323 K. This was to account for pre-heating of the baseplate and also to create a heat sink to represent the conductivity along the build direction. As the mechanical BC, the bottom surface of the baseplate was fixed in the displacement degree of freedom.

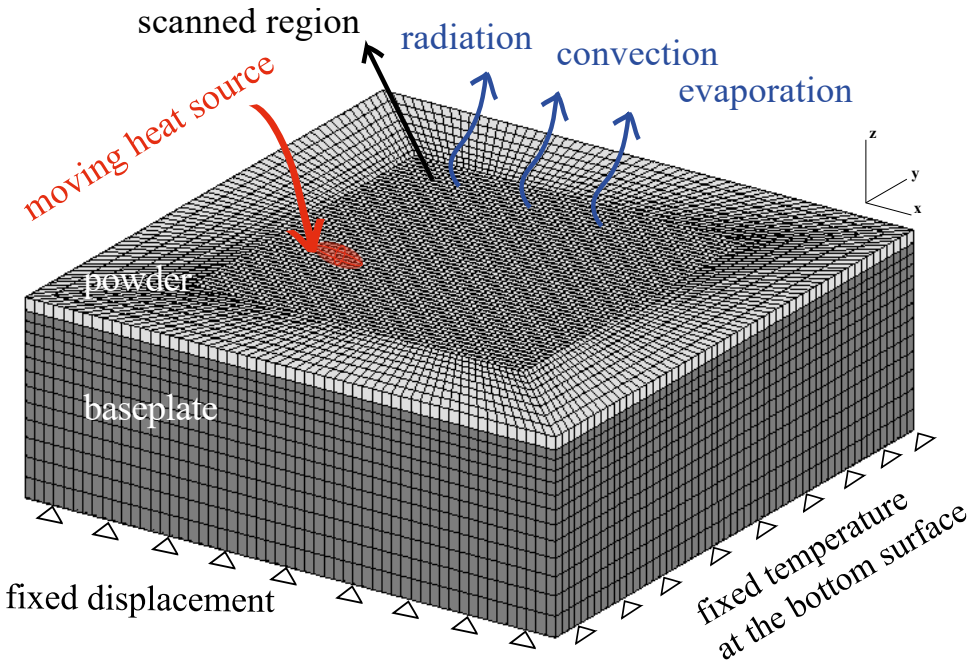

Figure 3-6 Mesh and boundary conditions in isometric view.

Figure 3-7 shows the FE model mesh from the top view. L_0 and W_0 were the scan vector length and hatched area width respectively. The hatched region was surrounded by a uniform fine mesh by a given offset value. The reason for this; since not just the deposition region but the whole heat-affected zone should have very fine mesh to avoid inaccurate results. The remaining part of the mesh was un-refined with a bias factor in all directions to decrease computational time. The hatched area was used as 1 mm^2 square in the analyzes. The baseplate dimensions were given in terms of the multipliers of the deposition volume in each direction. In this study, the baseplate was used 1.5 times larger than the hatched area in the x-y plane (1.5x1.5 mm). In the build direction (z-axis), the baseplate was 15 times larger than the height of the total deposited part. For example, for a single layer with a 40 μm thickness, 600 μm thick baseplate was used. For a single layer model consist of 68544 nodes and 62205 elements.

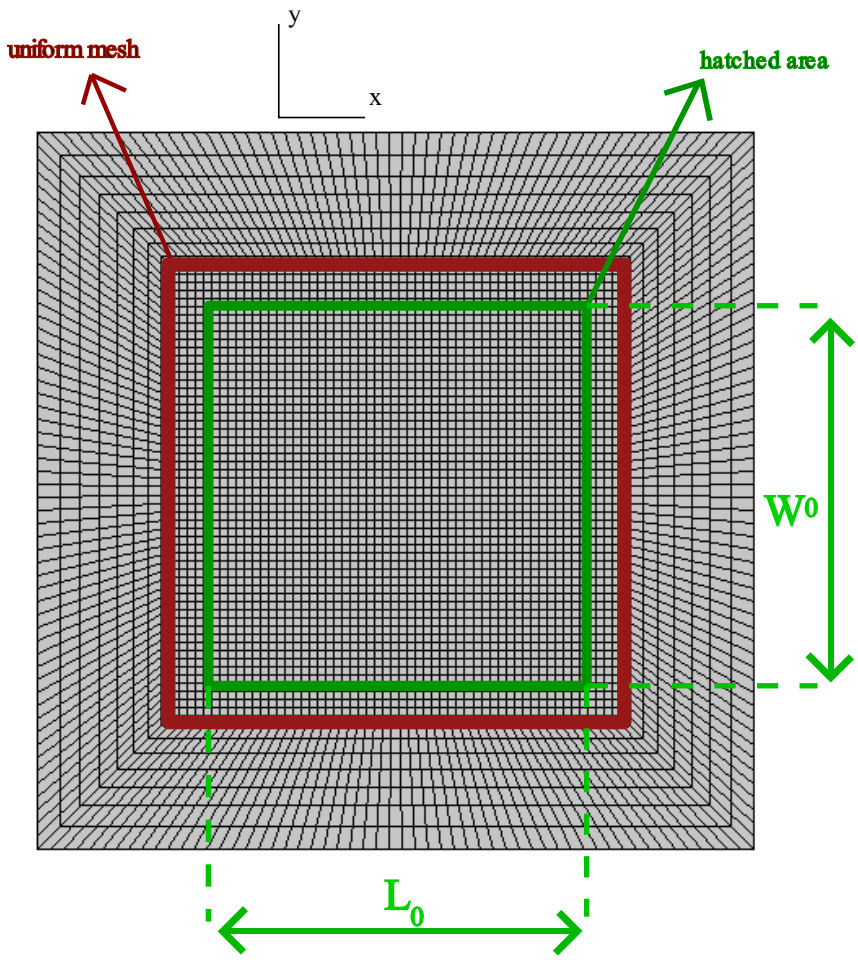

Figure 3-7: Top view of the FE model.

3.7 Mesh sensitivity study

The dimensions of the elements in the uniform fine mesh region were decided based on a mesh sensitivity study. The study was done for a single track on a single layer. The convergence study was conducted based on longitudinal and Von-Mises stresses, and maximum and minimum temperatures. Stress values were the average values over the deposited region, that were taken after the material cooled down to the steady-state temperature. Refinement was done for element dimensions in longitudinal and transverse directions. A reference value of 50 μm, which is equal to the radius of the laser beam was used. The dimension in the build direction (z-axis) was kept as the layer thickness for the elements in the deposited region.

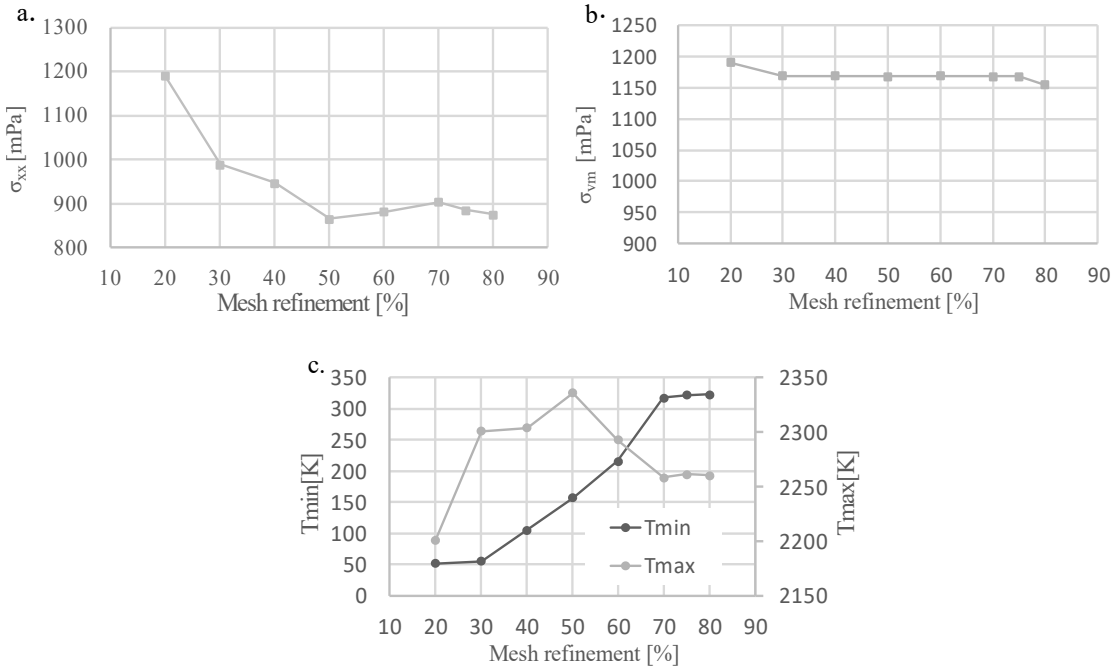

Figure 3-8: Mesh convergence study for average a. longitudinal stress, b. Von-Mises stress, and c. maximum and minimum temperatures.

As shown in Figure 3-8, the average Von-Mises was about the same during the refinement however, average longitudinal stress settled down to a steady value around %50 of refinement which was around 25 μm. The minimum temperature that occurred during

deposition was critical for the mesh refinement since it dropped below the baseplate temperature (323 K) around the HAZ, as shown in Figure 3-9. This was physically impossible due to the conservation of energy law. The reason for that inaccurate result was the intense heat source that was creating high thermal gradients over the low conductive powder. Considering the computational time, the %60 refinement was applied for the uniform fine mesh, which was equal to 20 μm element size in x and y directions. Besides, for the consecutive tracks, the minimum temperature was increasing to a reasonable value since deposited solid material has a higher conductivity that allowed temperatures to dissipate more easily.

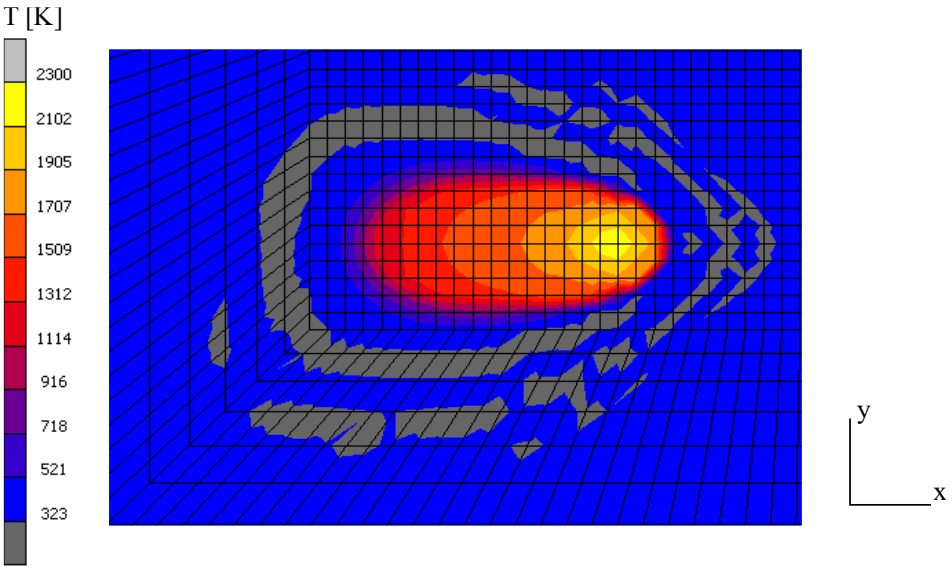

Figure 3-9: Heat affected zone with a mesh refinement of %50.

3.8 Time stepping scheme

The simulation consisted of three different time intervals which were scan time, dwell time, and recoating time. Scan time was to account for the deposition of a single scan vector. Between consecutive tracks, there were dwell time intervals to account for repositioning of the laser focus for the following track. After a layer was deposited, there was a recoating time that was around 0.1 s to simulate the recoating blade to spread the new layer of powder. Although in the real LPBF process, the time it takes for that is much longer, 0.1 s was enough for temperatures to become a steady-state value. After the end of a recoating time, elements of the following layer are activated.

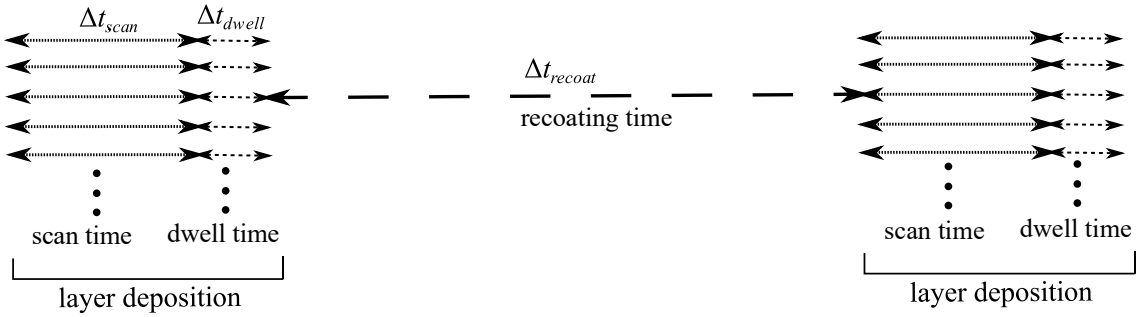

Figure 3-10: Time intervals and stepping scheme.

Scan time was divided into time increments of Δt_{scan}. The maximum Δt_{scan} could get was limited by the criterion that is shown in equation (3-48), to ensure that heat input does not skip and leave any undeposited region.

$$\Delta t_{scan} < \frac{r_x}{v} \tag{3-48}$$

Additional to that, the minimum value of the Δt_{scan} was set by the equation (3-49), where e is the minimum element size in the scan direction. This was to avoid the thermal shock effect that results in non-physical temperatures.

$$\Delta t_{scan} > \frac{e^2 \rho C_p}{k} \tag{3-49}$$

Time steps during intervals for the dwell and recoating times were adjusted accordingly length of the time. The recoating time was requiring much larger steps compared to others, hence it was adjusted accordingly in the subroutine UTIMESTEP, which is presented previously.

3.9 Scan path

Scan path was generated with an algorithm based on the total simulation time, and size of the hatched area. The methodology was valid for scanning rectangular hatches. The block diagram for the algorithm is shown in Figure 3-11 below. The algorithm was repeated for each time increment. The input was the total simulation time, *t*, and laser source was at the initial position coordinates; x_0, y_0, and z_0. Firstly, coordinate in the build direction (z-direction) was decided based on the total layer building time, t_{layer}. If time was greater than t_{layer}, coordinate of the laser was raised by the amount of the layer thickness, Δh, in the build direction. Next, the total time for scanning a single track (including dwell time) $t_{\text{scan track}}$ was used to compute coordinates of the laser beam in the x and y-axis at each time increment as described in the figure below.

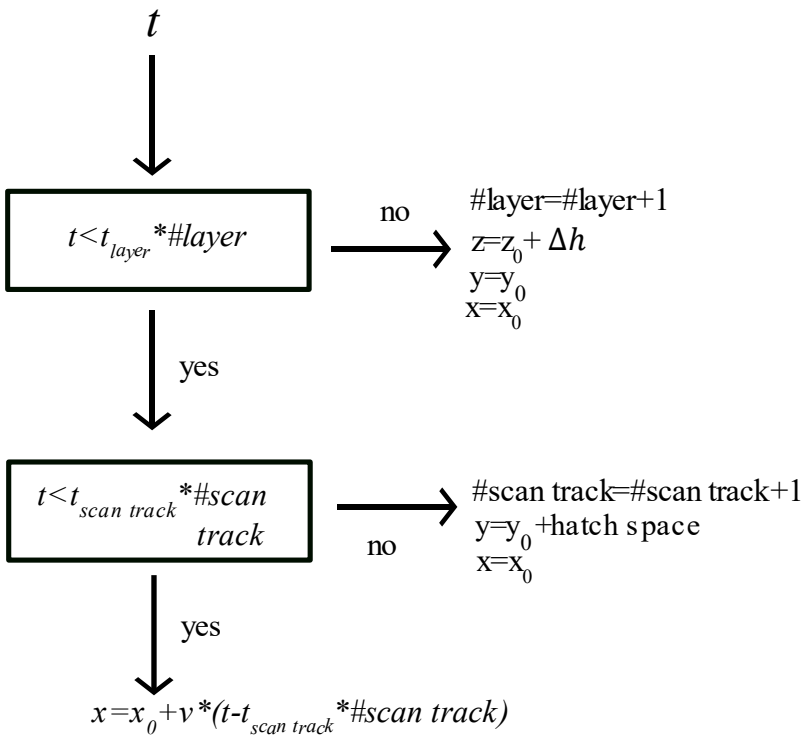

Figure 3-11: Scan path algorithm.

3.10 Summary

In this chapter, the methodology that was followed in the development of the FE model is described. Transient energy balance that comes from the conservation of energy was used as the governing equation for the thermal part of the model. For the mechanical model, the mechanical equilibrium condition must be satisfied. Since the problem was time-dependent and non-linear, the Newton-Raphson method was used through the commercial FEA software. MATLAB®, FORTRAN®, and MSC MARC® were used within an interaction. Subroutines that were written in FORTRAN® allowed implementations such as temperature dependent material properties, and user-defined elastic-perfectly plastic material model. Surface heat losses were represented as a volumetric input using Gauss's theorem, which can be a practical method for other AM simulations as well. A mesh sensitivity study was carried on the decision of element size in the region with a fine mesh. Lastly, process simulation was divided into different time intervals each consisting different time-stepping scheme.

4 EXPERIMENTAL VALIDATION OF THE THERMAL MODEL

To validate the thermal solution of the developed FE model, an experimental study was conducted. The experiment was done using the EOS M 290 LPBF machine located at Sabancı University Integrated Manufacturing Research and Application Center (SUIMC) as shown in Figure 4-1. Single tracks with 40 mm in length were deposited on a single layer using different laser power values. Each track was separated by 3 mm to avoid any interactions between them. The study was done for laser power values; 160, 190, and 220 W. On the other hand, scan speed was kept as default that was 960 mm/s.

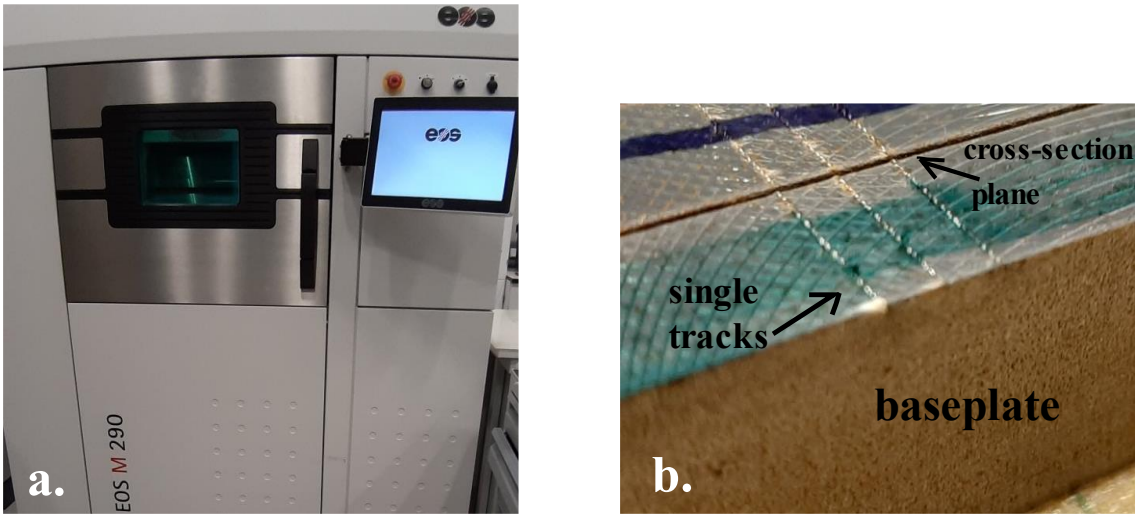

Figure 4-1: a. EOS M 290 LPBF system located in SU-IMC, b. samples after cross-sectioned with AWJ process.

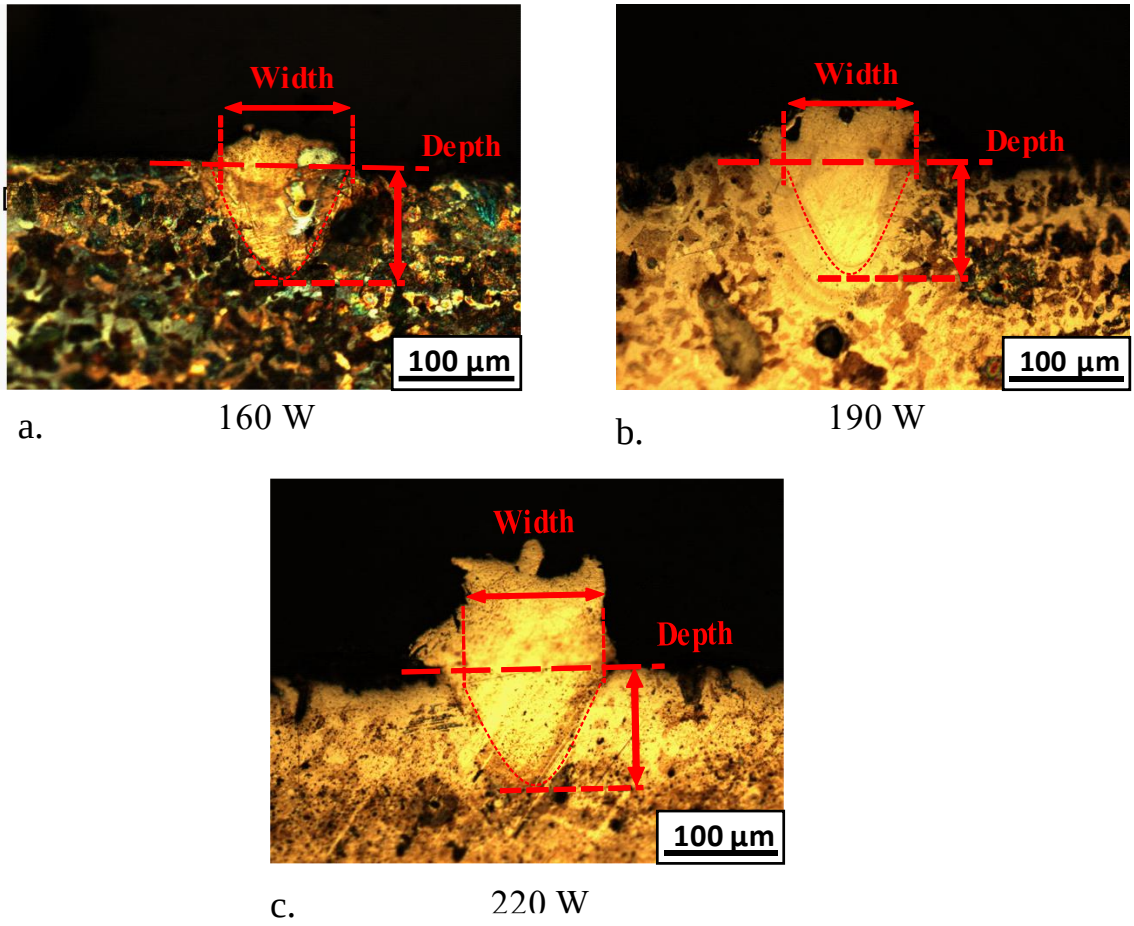

Figure 4-2: Melt pool images from the experimental study. Laser power values a. 160 W, b.190 W, and c. 220 W.

At first, stainless steel 316l baseplate was prepared and sterilized to avoid any oxidation during the process. The baseplate was preheated to 323 K by the machine and build chamber filled with argon gas until the required oxygen level was satisfied. The deposition material was Inconel 718® as it was used in the simulation. The layer thickness was 40 μm. Samples were prepared in Materialise Magics® as an STL file and transferred to the EOSPRINT® for adjusting the process parameters. Since laser beam diameter is approximately 100 μm, the width of the rectangular box models that were drawn in Materialise Magics® must be greater than the beam diameter. Otherwise, there wouldn't be any deposition occur at all.

After the samples were deposited, they were cross-sectioned perpendicular to the scan directions. This operation was done by the abrasive water jet (AWJ) cutting process. Metallographic cold mounting was applied to the cross sectioned samples via mixture of epoxy resin and hardener. Next, samples were wet polished with SiC grinding papers and then polished with 1 μm Aluminum oxide (Al203) suspension. Lastly, polished surfaces were etched with a mixture of hydrogen chloride, acetic acid and nitric acid and melt pool images were taken via Nikon LV1000ND optical microscope as shown in Figure 4-2. For measurement of the melt pool depth, baseplate level was taken as the reference, as it was done in the study by Zhang et al. [19].

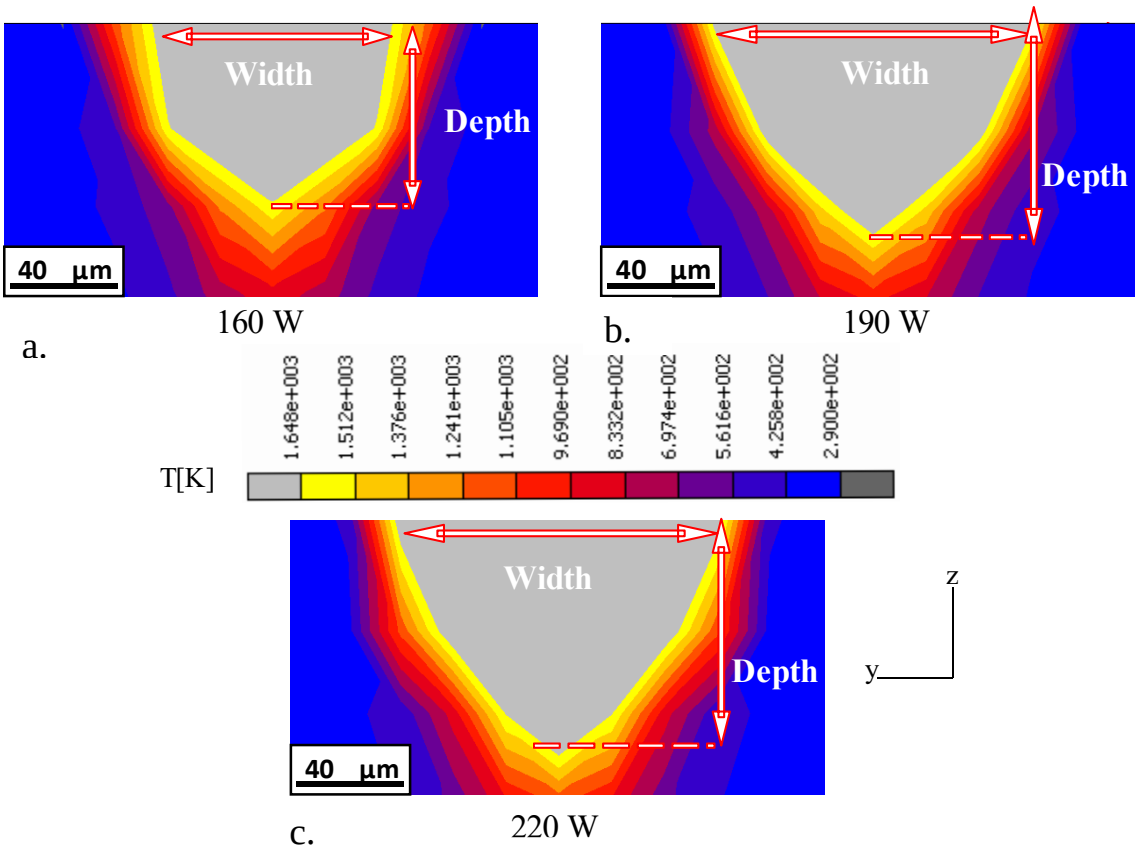

Figure 4-3: Cross-sections of melt pool from simulation results. Laser power values a. 160 W, b.190 W, and c. 220 W.

In Figure 4-3 melt pool cross-sections from the thermal simulation are shown. To replicate the experimental condition, simulations were done for a single track on a single layer with 40 μm thickness. Track lengths were kept as 1 mm in the simulation since it

was a sufficient distance for melt pool dimensions to reach a steady-state value [55]. The melt pool was identified by the temperature contour as shown as grey color in the figure. A raster graphics editor was used to compute the dimensions of the melt pool from the images from both experimental and simulation results. Experimental data was measured 10 times to gather the measurement uncertainty and %99 confidence level was used.

Table 4-1: Comparison of melt pool dimensions, experimental vs simulation.

laser power	scan speed	layer thickness	width			depth		
			exp.	sim.	err.	exp.	sim.	err.
[W]	[mm/s]	[µm]	[µm]	[µm]	%	[µm]	[µm]	%
160	960	40	116 ± 2	122	+5.2	68± 2	74	+8.8
190	960	40	125 ± 4	128	+2.4	88± 4	81	-7.9
220	960	40	138 ± 3	144	+4.3	95± 2	89	-6.3

Table 4-1 shows the comparison of experimental and simulation data in terms of melt pool width and depth. The maximum error occurred in the prediction of melt pool depth while using the laser power as 160 W. It was overpredicted with an amount of %8.8 by the model when it was compared to the experimental results. Besides, for all parameters predicted melt pool dimensions were within the range of %10 deviation from the experimental data. Considering there could be some small deviations on the laser beam radius and in the thickness of the layer as well, the resulting error was acceptable, and the thermal model was in good agreement with the experimental results on the prediction of melt pool dimensions.

5 A PARAMETRIC STUDY USING THE THERMOMECHANICAL MODEL

In this chapter, analyzes that were made on a single layer deposition are presented. The influence of process parameters on the thermal behavior and residual stresses were investigated. Four process parameters that were laser power, scan speed, hatch spacing, and layer thickness were used for the analysis. Hatch spacing is the space between consecutive tracks. Moreover, unidirectional and zigzag scan patterns were compared. Parameters were selected as commonly used ones in the LPBF process with EOS M 290 machine [56]. Parameters are summarized in Table 5-1 shown below. While altering any of the parameters, the remaining ones were kept constant to investigate the effect on each parameter individually.

Table 5-1: Parameters that are investigated

laser power	scan speed	hatch spacing	layer thickness	scan pattern
P	v	Δd	Δh	-
[W]	[mm/s]	[μm]	[μm]	-
160	600	75	30	unidirectional
190	1000	90	40	zigzag
220	1200	100	50	

5.1 Thermal analysis

Figure 5-1 and Figure 5-2, show the distribution of temperature and material phase, respectively, when simulation time, *t*, was at 0.00899 s and 8th consecutive track was being scanned. Process parameters were laser power as 160 W, scan speed as 1000 mm/s, hatch spacing as 90 μm, and layer thickness as 40 μm. A unidirectional scan pattern was used along the x-axis. As it is shown, the temperature was concentrated over the deposited

region, rather than dissipating through the powder. The reason for that was the conductivity difference between powder and solid phases of the material as highlighted before. Especially along the y-direction, high thermal gradients occur because of this reason. While undeposited powder was at around the initial temperature (323 K), the temperature at the center of the laser beam was exceeding 2000 K.

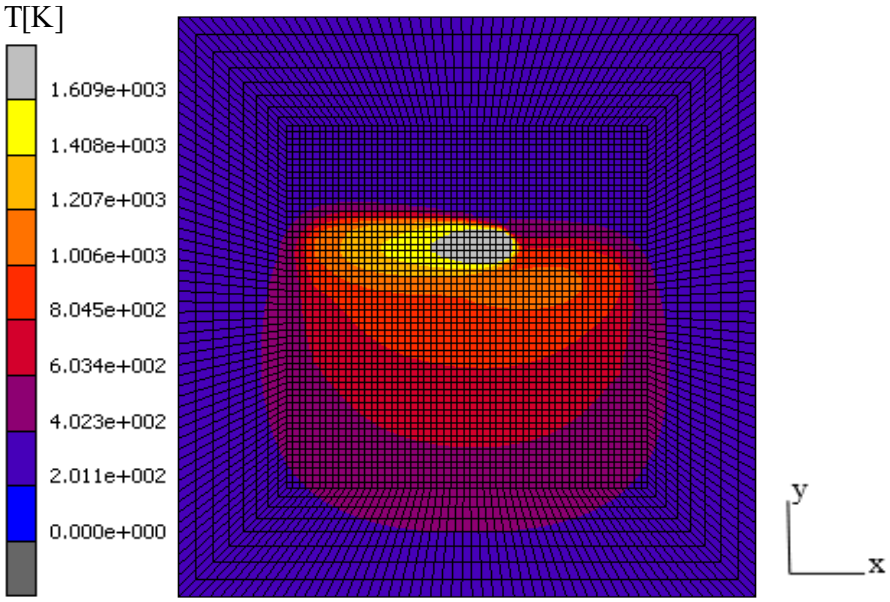

Figure 5-1: Temperature distribution at *t*=0.00899 s.

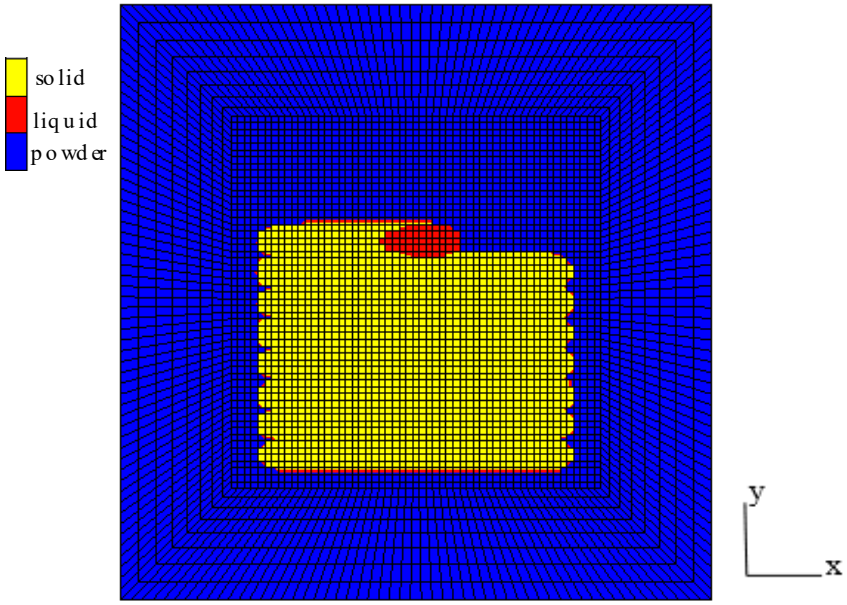

Figure 5-2: Phase distribution at *t*=0.00899 s.

The effect of process parameters on the dimensions of the melt pool was investigated as shown in Table 5-2. The dimensions were extracted as explained in Chapter 4 with a raster graphics editor. However, in contrast to the previous chapter, this time melt pool dimensions were extracted while laser scan was at the middle of the hatched region while multiple tracks were deposited already. This was to observe the effect of hatch spacing parameter as well. Altering the laser power expanded or contracted the melt pool in all directions at approximately the same rate. On the other hand, variation in scan speed changed the aspect ratio of the melt pool. When the scan speed was increased, total energy input decreased, and it caused to depth, width, and length of the melt pool to became smaller. However, at the same time since the laser was traveling faster in the scan direction (x-axis) and forced the length of the melt pool to increase as well. These two effects counteracted each other. The width to length and depth to length ratios of the melt pool geometry varied with the scan speed, whereas aspect ratios were almost the same while altering the laser power. Depth of the melt pool was slightly increased when hatch spacing was decreased because of the overlapping with the previously melted track. Increasing the layer thickness did not cause any significant changes in the melt pool dimensions.

Table 5-2: Melt pool dimensions for varying process parameters.

laser power [W]	scan speed [m/s]	hatch spacing [µm]	layer thickness [µm]	width [µm]	depth [µm]	length [µm]
160	1000	90	40	124	77	276
190	1000	90	40	130	86	333
220	1000	90	40	149	93	402
160	600	90	40	160	95	284
160	1200	90	40	121	68	272
160	1000	75	40	122	81	274
160	1000	100	40	127	78	281
160	1000	90	30	121	72	265
160	1000	90	50	123	76	283

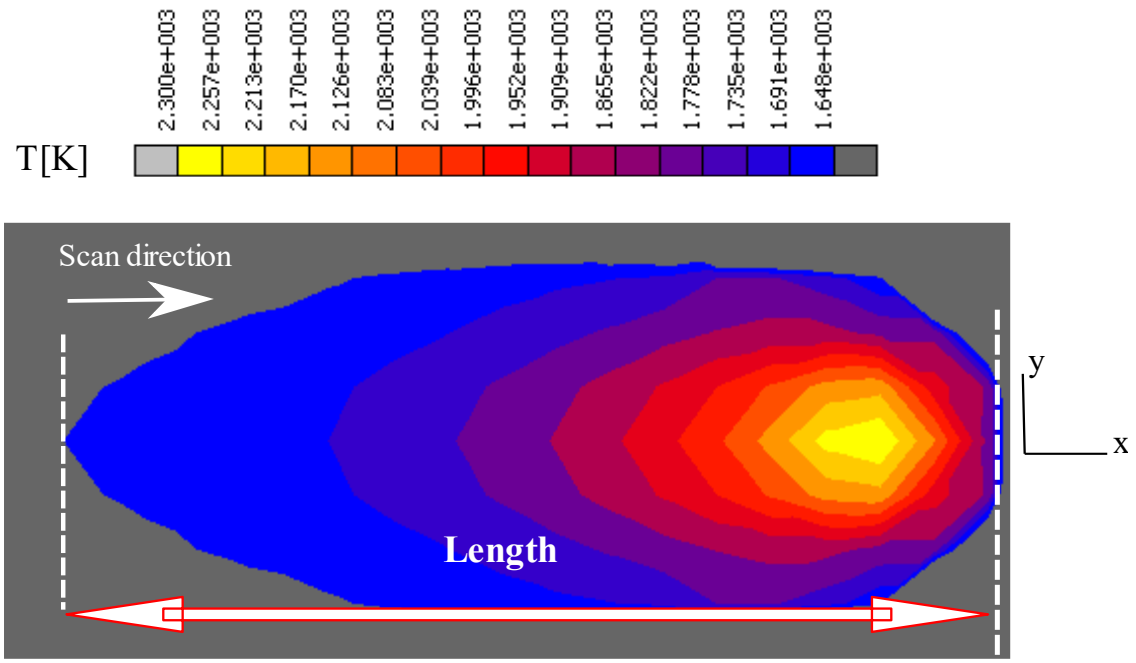

Figure 5-3: The melt pool from the top view.

The top view of the melt pool and temperatures within it are shown in Figure 5-3 above. The influence of laser power, scan speed, and layer thickness on the maximum temperature that was achieved during deposition are shown in Figure 5-4, Figure 5-5, and, Figure 5-6 respectively. There was a direct proportionality between maximum temperature, T_{max}, and the laser power as it is expected. Altering the power from 160 to 220 W caused approximately 400 K increase in the maximum temperature. A similar variation in the maximum temperature was observed when the scan speed was doubled, from 0.6 to 1.2 m/s. Increasing the layer thickness decreased the maximum temperature slightly since the same energy input was applied to a larger volume. On the other hand, a significant change was not observed while the hatch spacing was changed.

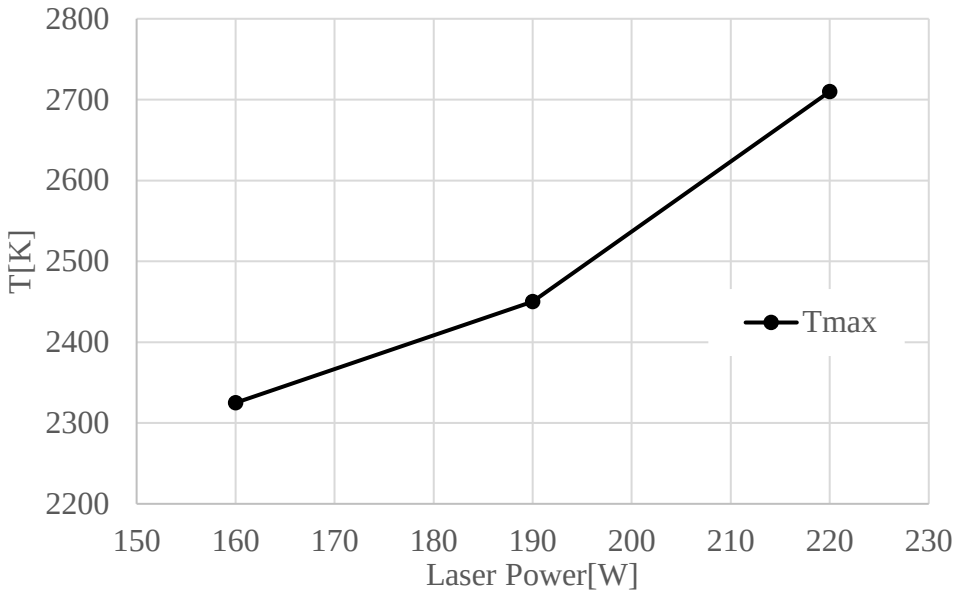

Figure 5-4: Maximum achieved temperature during deposition against varying laser power.

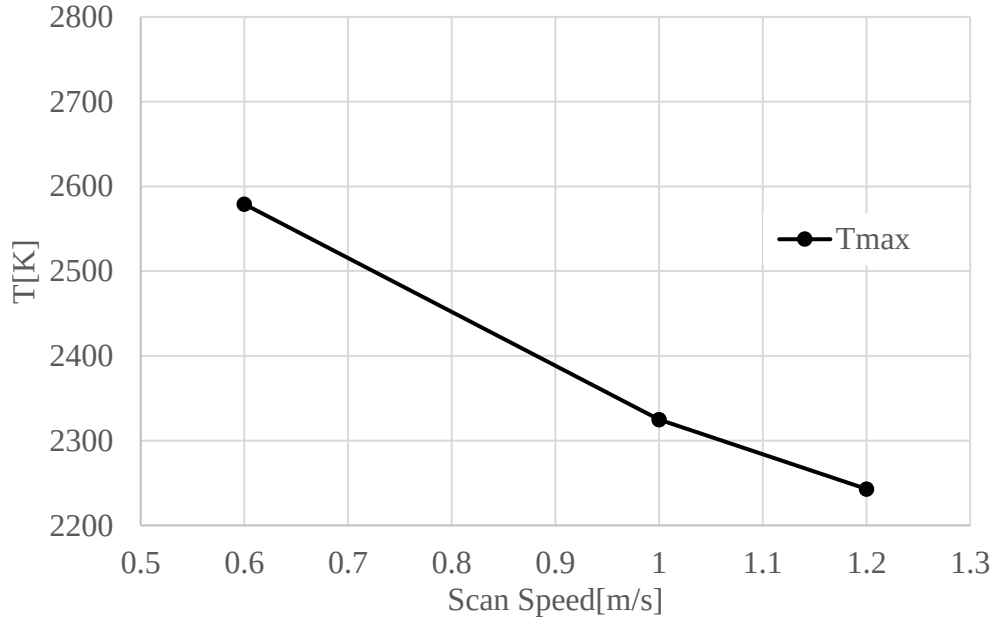

Figure 5-5: Maximum achieved temperature during deposition against varying scan speed.

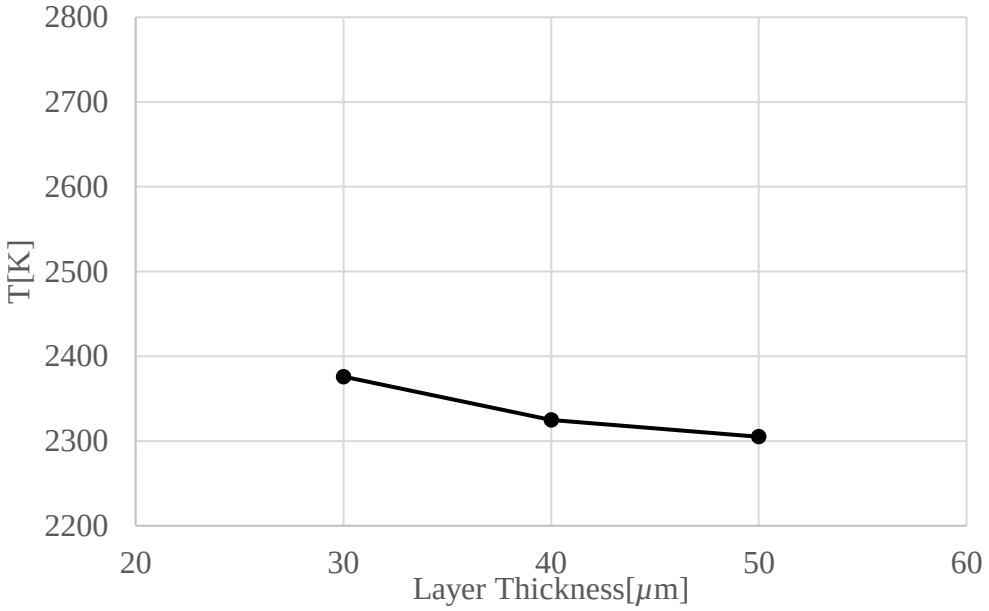

Figure 5-6: Maximum achieved temperature during deposition against varying layer thickness.

5.2 Mechanical analysis

Residual stresses that were left within the material after the deposition was completed were analyzed for varying process parameters. Only normal components of stresses in the longitudinal (σ_{xx}) and transverse (σ_{yy}) directions were involved in the discussion since other components were relatively small in magnitude as shown in Figure 5-11. Moreover, Von-Mises stresses were also compared according to altering parameters. The mentioned stress components were extracted from the surface of the deposited area and they were the average values. Figure 5-7, Figure 5-8, Figure 5-9, and Figure 5-10 show the impact of laser power, scan speed, hatch spacing, and layer thickness on the residual stresses respectively. Longitudinal stresses were the same and around the yield stress for almost all the process parameter combinations. The only exception was the layer thickness where both longitudinal and transverse stresses decreased when a thicker layer was used. The reason for this is; although similar thermal loads were applied for all layer thickness sizes, since their volumes differed among themselves, due to the nature of FEA, the stresses varied inversely with this volume change. Average transverse stresses increased with the laser power since thermal gradients became even greater with larger temperatures

occurring within the melt pool. Similarly, with a lower scan speed, the magnitude of transverse stresses got larger. Although alternation of the scan speed drastically influenced the total energy input and maximum temperatures as discussed before, its effect on transverse stresses was smaller compared to the effect of the laser power. Since the thermal gradient mechanism was also dependent on the melt pool geometry. As mentioned, the geometry of the melt pool was sensitive to the scan speed, the aspect ratio of the melt pool was directly affected by the parameter scan speed. The variation in the aspect ratio of the melt pool and HAZ, was influencing the thermal gradient mechanism independent of the energy input. According to the simulation results, no clear relationship was found between hatch spacing and stresses. However, it should be noted that metallurgical bonding and microstructure effects were excluded in this meso-scale model. Von-Mises (or equivalent) stresses followed a similar trend with the longitudinal and transverse stresses since they were the dominant components as also can be seen in Figure 5-11. The reason for that was the constraints in longitudinal and transverse directions were strong due to surrounding deposited and material and prevent contraction and causes residual tensile stresses to build up. This mechanism is discussed in the next chapter in more detail. For all the parameter combinations, stresses parallel to scan direction were around 1.5 times larger than the ones in the perpendicular direction, as also concluded in other studies [42], [57].

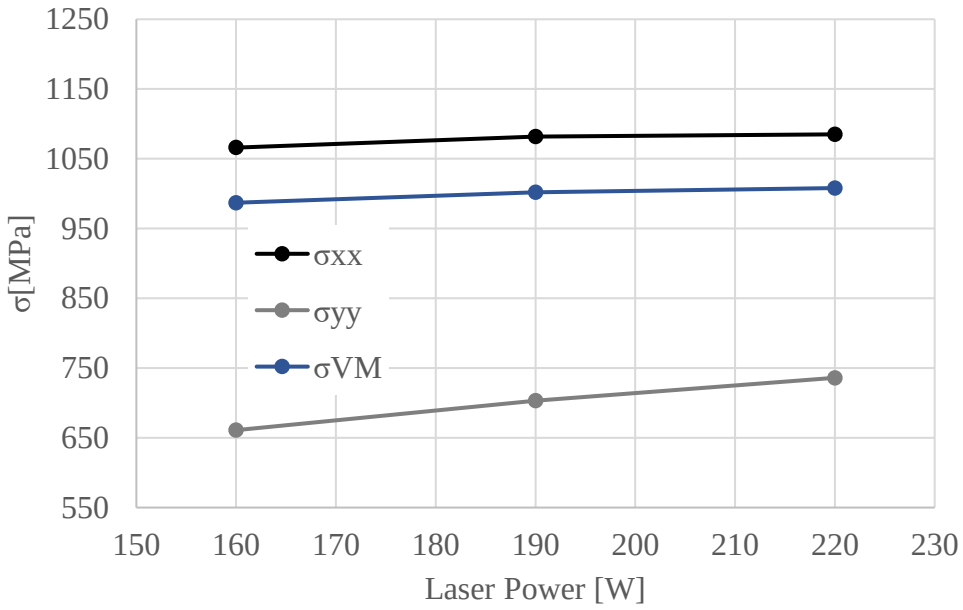

Figure 5-7: Longitudinal, transverse, and Von Mises stress against varying laser power.

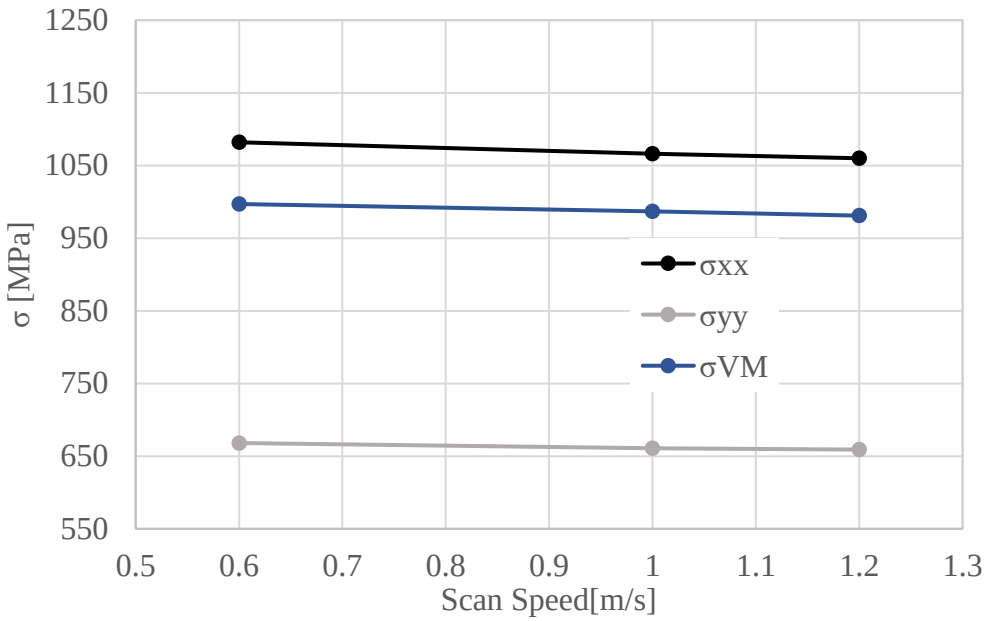

Figure 5-8: Longitudinal, transverse, and Von Mises stress against varying scan speed.

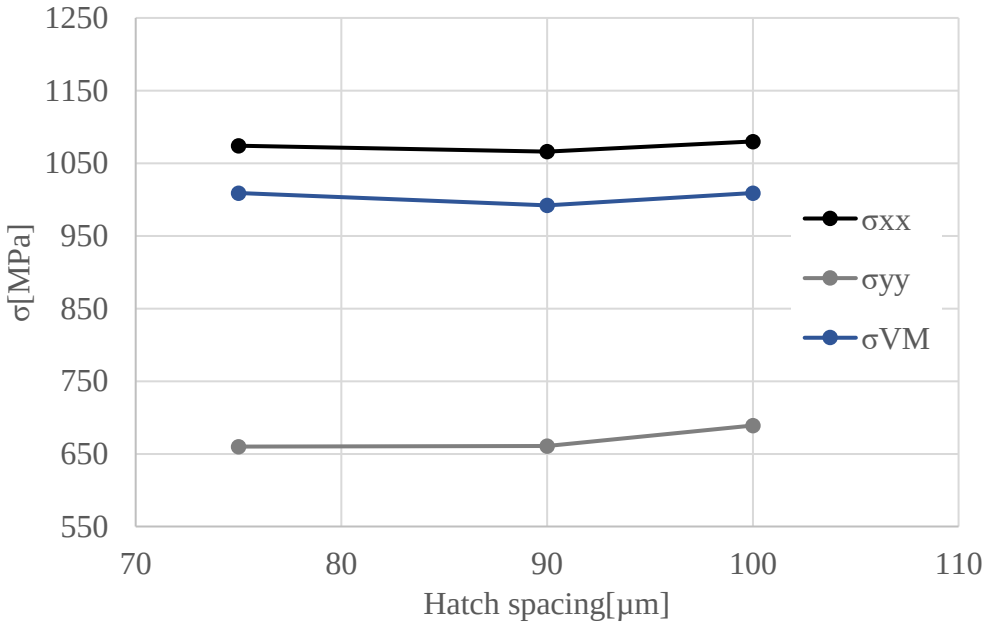

Figure 5-9: Longitudinal, transverse, and Von Mises stress against varying hatch spacing.

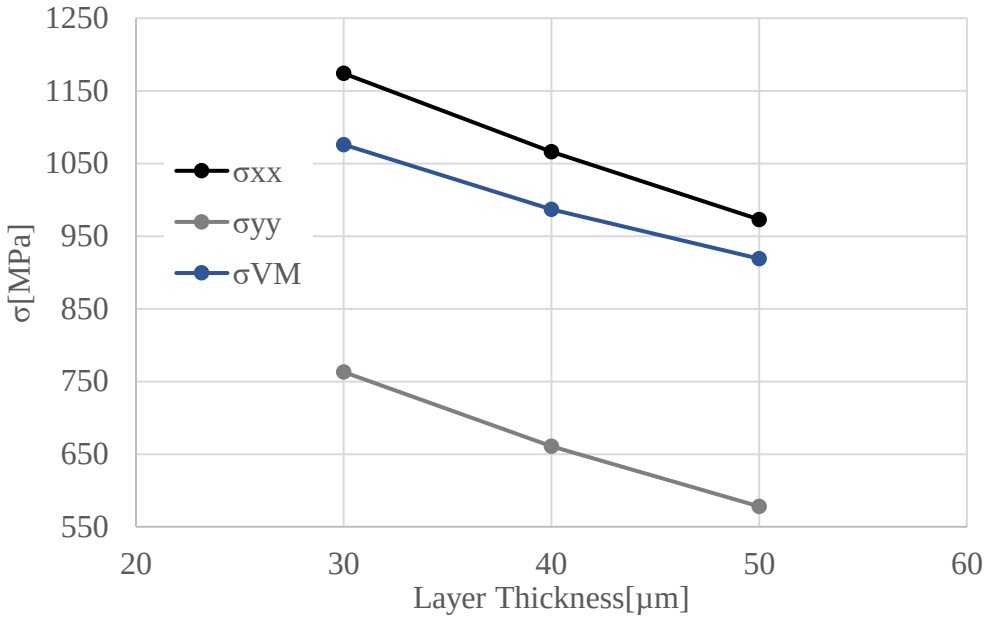

Figure 5-10: Longitudinal, transverse, and Von Mises stress against varying layer thickness.

All the six stress components are shown in Figure 5-11 below. These were the stresses that were left after the deposition of the first layer and the material was cooled down to a steady-state temperature. The deposition was done with the parameters as follows; laser power as 160 W, scan speed as 1 m/s, hatch spacing as 90 μm, and layer thickness as 40 μm. A unidirectional scan pattern was used. As mentioned, longitudinal and transverse components were much greater than the remaining stress components. The normal component of stress along build direction and shear stresses were very low in magnitude over the deposition region. The only places that they were getting relatively greater were boundaries of the solidified deposition region and powder. The powder phase of the material had a very low modulus of elasticity, so it could deform very easily and did not carry any stresses at the same time. However, boundaries of the deposited region where transitions occurred from stiff deposited Inconel 718® to soft powder phase, which created some kind of stress concentrations due to high deformation of powder elements. However, they did not have any impact on the hatched region, hence were not included in the discussion.

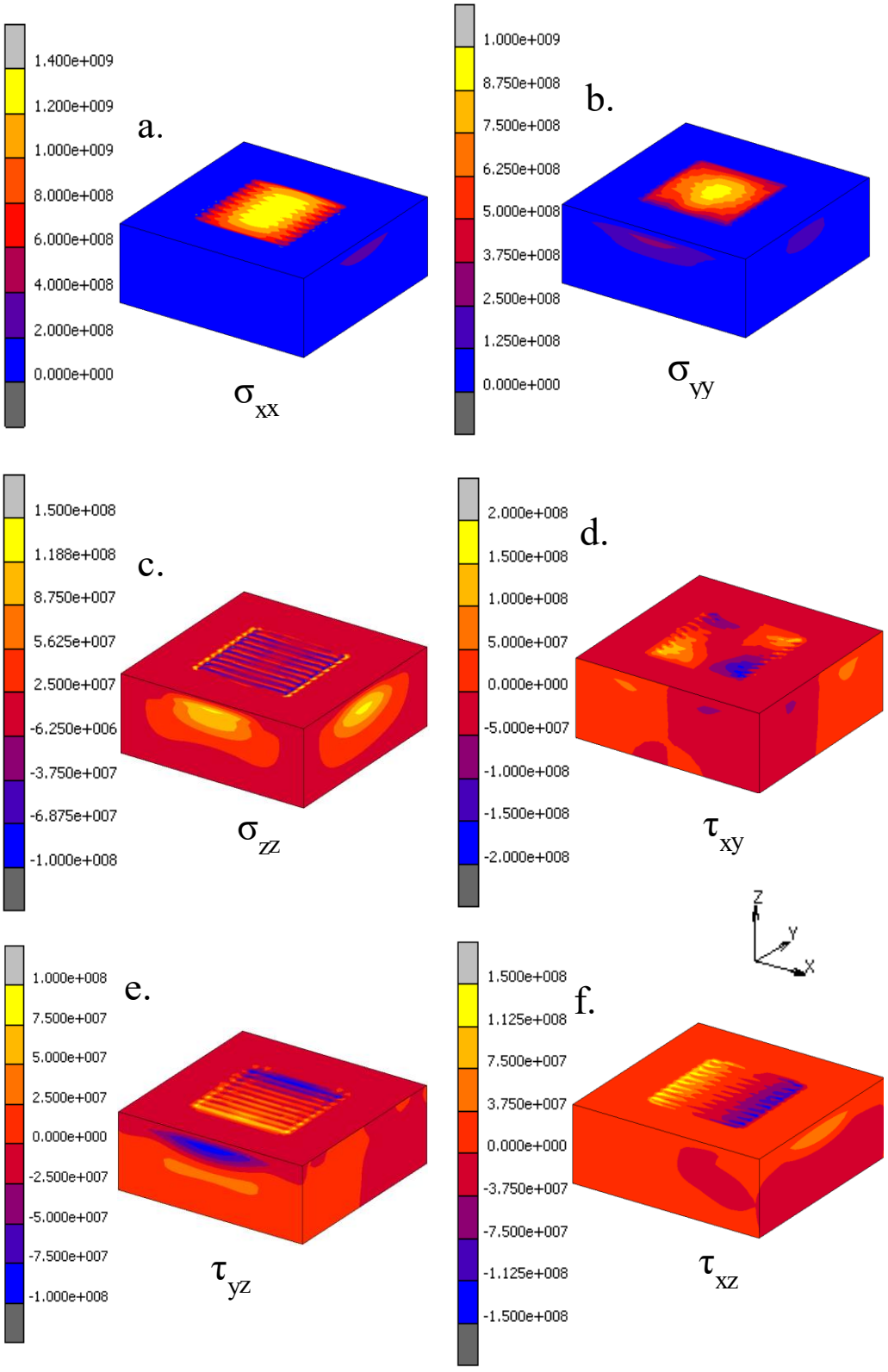

Figure 5-11: Stresses after the deposition of the first layer a. σ_{xx}[MPa] b. σ_{yy}[MPa] c. σ_{zz}[MPa], d. τ_{xy}[MPa] e. τ_{yz}[MPa] f. τ_{xz}[MPa].

A comparison was made on the unidirectional and zigzag scan patterns based on the residual stresses as shown in Figure 5-12. Both scan patterns formed similar stresses in terms of magnitude. On the other hand, there were slight deviations in terms of the distribution of these stresses, especially at the near ends of scan tracks. The reason for that is the changing thermal gradient mechanism with the scan pattern. While scanning with a zigzag pattern, the following scan track begins nearby at where the latter track is ended. Therefore, thermal gradients become smaller due to the previously heated region, and stresses are slightly reduced. By contrast, the region that this following track ends, cools down until the laser source. As a result, this time thermal gradients get larger because of the relatively cooled down surroundings. This mechanism was repeated for every two scan tracks which resulted in altering high and low stress fields at near ends of the scan tracks.

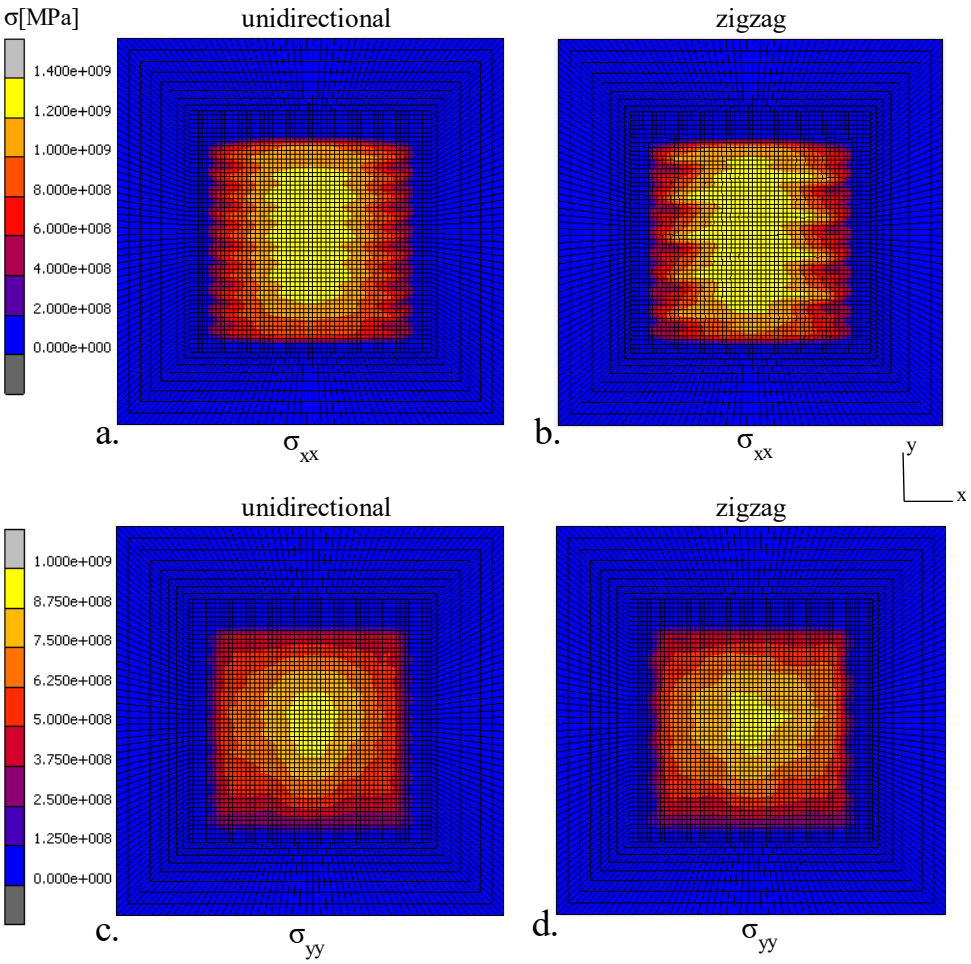

Figure 5-12: Stress results using different scan patterns. a. σ_{xx} from unidirectional, b. σ_{xx} from zigzag, c. σ_{yy} from unidirectional, and d. σ_{yy} from zigzag patterns.

5.3 Summary

A parametric study that was conducted on the developed thermomechanical finite element model is described in this Chapter. The analyzed parameters were laser power, scan speed, hatch spacing, and layer thickness. Moreover, a comparison was made between unidirectional and zigzag scan patterns. The parameters were compared with respect to the maximum temperature that was achieved during the process, melt pool dimensions, and residual stresses that were left after the deposition. All these four parameters are often used together to formulate the total energy input. However, according to results, laser power and scan speed were the primary parameters that influenced the maximum temperature that occurred during deposition. Laser power and scan speed also significantly shifted the dimensions of the melt pool. Not only the size, but the geometry of the melt pool also got affected with alternation of the scan speed. Normal components of stresses in longitudinal and transverse directions were dominant components over the other components of stress. According to the simulation results, the selection of layer thickness and laser power could significantly affect residual stresses. There were no significant differences between unidirectional and zigzag scan patterns in terms of the magnitude of stresses, but stress distribution varied slightly.

6 FAST PREDICTION OF RESIDUAL STRESSES USING STRESS BASED INHERENT STRAIN METHOD

Computation of stresses with a thermomechanical elastic-plastic analysis could be accurate but computationally costly. Moreover, due to the soft powder material phase, computations could get even more challenging. As a result, often new methods and applications are sought by researchers to predict these stresses without conducting a full simulation. In this chapter, at first, the original inherent-strain method for welding simulations is discussed. Then a practical stress-based modified approach is presented which was developed for the quick prediction of residual stresses using only thermal analysis. The results of the method were compared with the fully elastic-plastic thermomechanical solution.

6.1 Inherent strain method

The inherent strain method (ISM) was developed to be used in the welding simulations as discussed in Chapter 1. In this sub-section, the methodology that was presented by Luo et al. is explained [58]. The incompatible strains that cause stresses in thermally induced processes such as welding and the LPBF are often called inherent strains. They are used to estimate deformations and residual stresses. In this method, inherent strains, ϵ_{IS}, are computed based on the maximum achieved temperature T_{max} of a material point as shown in equation (6-1), where β is the constraint at each direction, which is a value between 0 to 1, depending on the stiffness. Constraints restrict the expansion and contraction of a material point during a thermal cycle. T_1 and T_2 are the temperature criteria that are dependent on the material properties and constraint as shown in equation (6-2).

$$\epsilon_{IS} = \begin{cases} 0, & T_{max} \le T_1 \\ -\alpha T_{max} + \dfrac{Y}{E\beta}, & T_1 < T_{max} \le T_2 \\ -\dfrac{Y}{E\beta}, & T_2 < T_{max} \end{cases} \quad (6\text{-}1)$$

$$T_1 = \frac{Y}{E\alpha\beta} + T_0\,, \quad T_2 = 2T_1 \quad (6\text{-}2)$$

The theory behind equation (6-1) comes from the mechanism that is illustrated in Figure 6-1 below, which shows a stress-strain diagram of a material point under the heating-cooling cycle. During heating compressive elastic strains develop since surrounding constraints prevent thermal expansion of the material. The material does not experience any plastic deformations or residual stresses until point P1, where T_{max} equals to T_1.

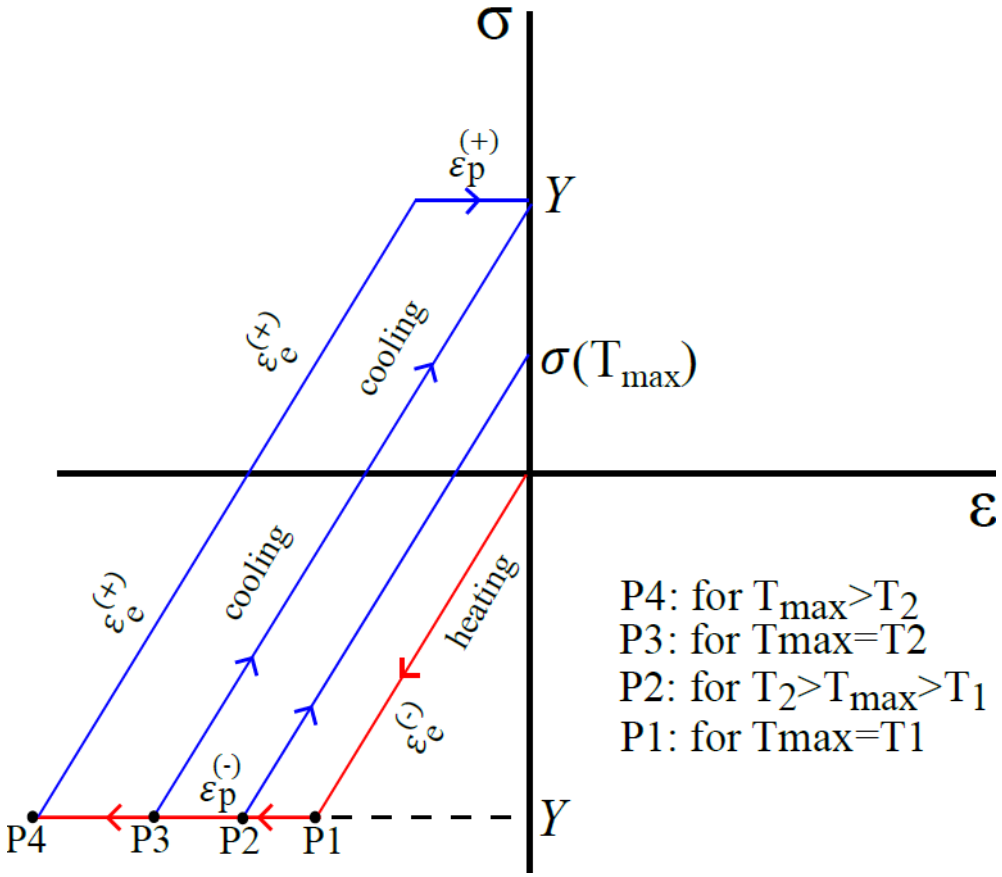

Figure 6-1: Stress-strain diagram of a material point under thermal cycle with constraints.

However, when T_{max} exceeds T_1, material yields and deforms plastically. Then, at the cooling stage material contracts but since surrounding constraints restrict shrinkage, tensile stresses build up and are left within the material as tensile residual stresses and compressive plastic strains. The magnitude of tensile residual stresses and compressive inherent strains increases with T_{max}, since thermal expansion and shrinkage rate becomes greater. However, at the instant when T_{max} reaches to the criteria T_2, material yields and deforms plastically also during the cooling stage. Hence residual stress and inherent strain become equal to the yield stress and strain respectively, independent of T_{max}.

The theory is used to calculate inherent strains in the longitudinal direction, $\epsilon_{IS_{xx}}$, as shown in Equation (6-3). Longitudinal is referred to as welding or scan direction and β_x is the constraint in that direction. Similarly, to compute inherent strains in the transverse direction, $\epsilon_{IS_{yy}}$, equation (6-4) is used. In this equation, *A* is an unknown constant and *C* equals to T_2. The latter comes from the continuity condition of the equation. The difference in the formulation to compute transverse inherent strains comes from the fact that constraint along the transverse direction is much looser than the one in the longitudinal direction ($\beta_x \gg \beta_y$). Consequently, temperature criteria also differ for each direction, such as T_{1y} is greater than T_{2x}. Hence, T_{max} is assumed to be either less than T_{1y}, or between T_{1y} and T_{2y} for transverse direction. As a result, inherent strains are always a function of T_{max}, as described in equation (6-4). Inherent strain in the build direction (z-direction) can be computed from incompressibility condition. In the original method, inherent strains are computed and extracted from an elastic-plastic thermomechanical simulation and then an elastic FE analysis is carried to predict residual stresses.

$$\epsilon_{IS_{xx}} = \begin{cases} 0, & T_{max} \leq T_{1x} \\ -\alpha T_{max} + \dfrac{Y}{E\beta_x}, & T_{1x} < T_{max} \leq T_{2x} \\ -\dfrac{Y}{E\beta_x}, & T_{2x} < T_{max} \end{cases} \qquad (6\text{-}3)$$

$$\epsilon_{IS_{yy}} = \begin{cases} 0, & \mathrm{T_{max}} \leq \mathrm{T_2} \\ -\mathrm{A}\alpha(\mathrm{T_{max}} - \mathrm{C}), & \mathrm{T_2} < \mathrm{T_{max}} \end{cases} \qquad (6\text{-}4)$$

6.2 Stress based approach

In the present study, a different approach was taken for the application of the inherent strain method. This method uses the same theory that is explained in the previous sub-section with Figure 6-1. Here, residual stresses were directly predicted using T_{max} values of each integration point of a finite element. The normal components of residual stresses in longitudinal and transverse directions were computed from equations (6-5) and (6-6) respectively. As discussed, residual stresses become yield stress when T_{max} exceeds T_{2x}. Since for the deposited material, T_{max} is always larger than T_{2x}, residual stresses in the scan direction, S_{xx}, were assumed to be always yield stress on the hatched region. The normal stresses in the transverse direction, $S_{yy,}$ were function of T_{max}. They were in the region between P1 and P3 that are shown in Figure 6-1, where both residual stresses and inherent strains increased with T_{max}. The stresses in the build direction was relatively small due to loose constraints in that direction, which was shown in the previous chapter from the results of the thermomechanical simulation.

$$S_{xx} = \begin{cases} 0, & T_{max} \leq T_{1x} \\ Y, & T_{2x} < T_{max} \end{cases} \tag{6-5}$$

$$S_{yy} = \begin{cases} 0, & T_{max} \leq T_{2x} \\ A_s E \alpha (T_{max} - C), & T_{2x} < T_{max} \end{cases} \tag{6-6}$$

A_s, is another unknown that was found by calibration with elastic-plastic thermomechanical simulation. The calibration was done for three different laser power values which were 160, 190, and 220 W. For each analysis, the maximum normal stress in transverse direction plotted against T_{max}. At the end, A_s was computed as a function T_{max}. Then, the magnitudes of maximum residual stresses could be computed in the scan and transverse directions using T_{max}. However, for the distribution of them along the x-y plane, additional consideration had to be done, since stresses were distributed over deposited area as could be seen from thermomechanical results in Chapter 5. The

distributions of residual stresses were extracted from the thermomechanical simulation result, which is shown in Figure 6-3. Longitudinal stresses were assumed to be varying only through scan direction and do not change along the transverse direction. On the other hand, the variation of transverse stresses in both longitudinal and transverse directions was considered. Variations of stresses were captured by plotting in terms of normalized stresses ($\sigma_{xx}^{*}, \sigma_{yy}^{*}$) over the normalized scan vector length (L^{*}), and normalized hatched area width (W^{*}), as shown in Figure 6-3. This allowed to gather the distribution of stresses along scan vector length and hatched area width.

Figure 6-2 summarizes the procedure of the stress based inherent strain method that was used in this study. Firstly, magnitudes and distribution of residual stresses were extracted from the fully elastic-plastic thermomechanical simulation. Next, constant A_s was calibrated using three different laser power values to relate T_{max} with S_{yy}. These processes were done only once. Then, for any process parameter combination, only thermal analysis was needed to be solved to gather T_{max} so that magnitudes and distribution of residual stresses were obtained for a hatched area.

$$\sigma_{xx}^{*} = \frac{\sigma_{xx}}{\sigma_{xx}^{max}}, \qquad \sigma_{yy}^{*} = \frac{\sigma_{yy}}{\sigma_{yy}^{max}}, \qquad L^{*} = \frac{L}{L_0}, \qquad W^{*} = \frac{W}{W_0} \tag{6-7}$$

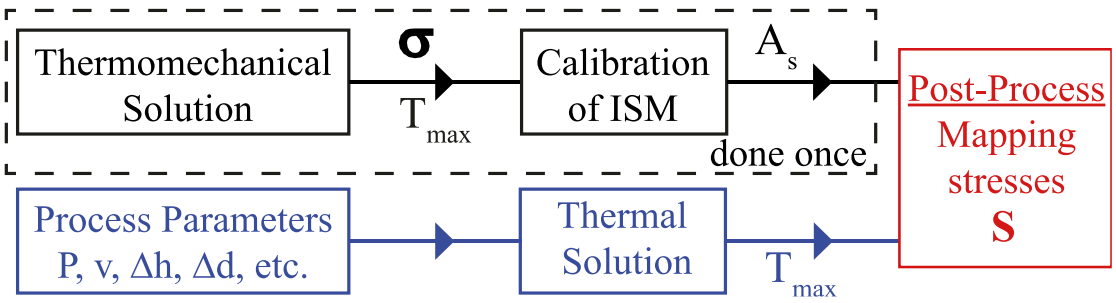

Figure 6-2: ISM application procedure.

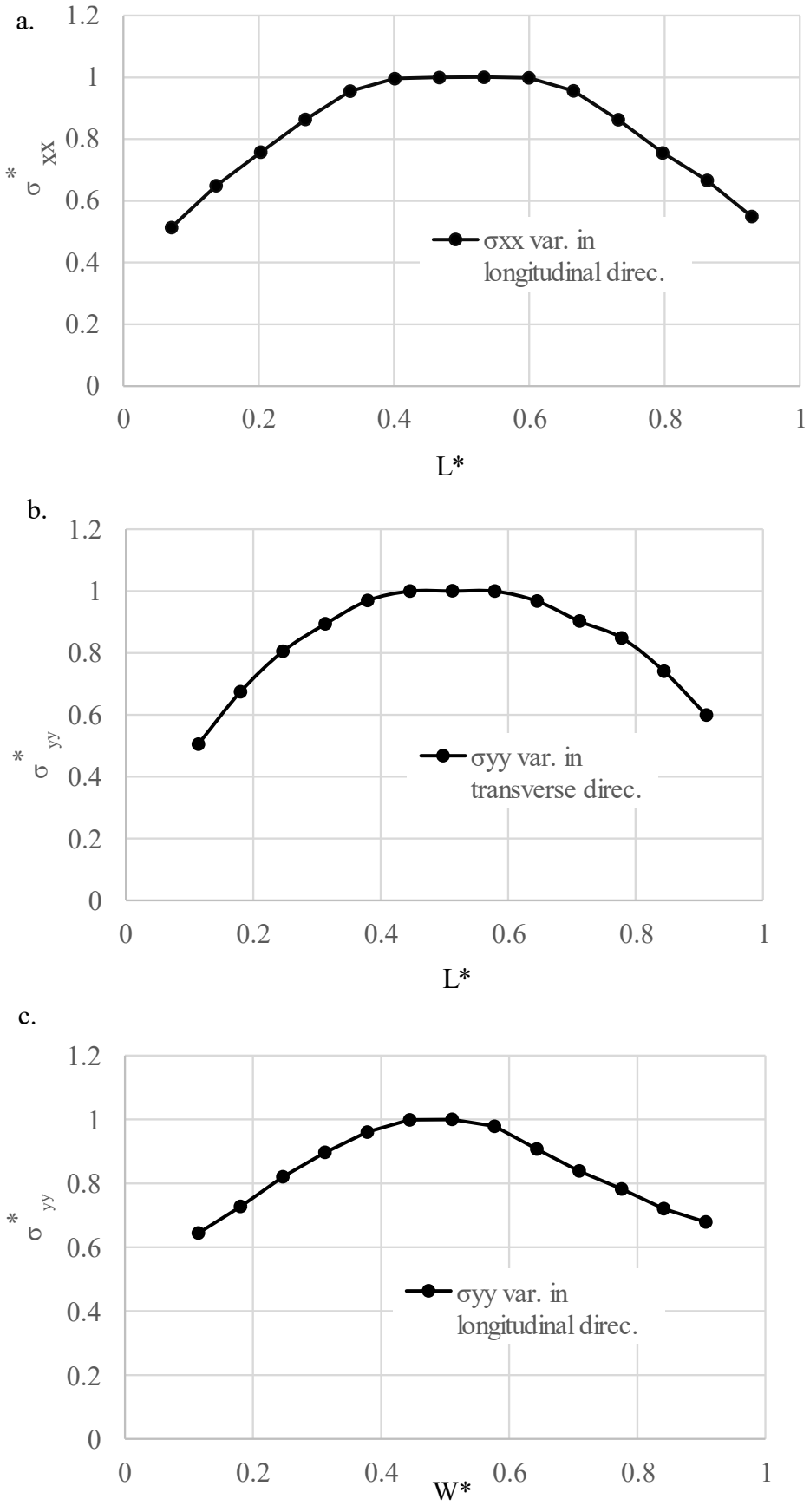

Figure 6-3: Variation of stresses; a. σ_{xx} in longitudinal direction, b. σ_{yy} in longitudinal direction, c. σ_{yy} in transverse direction.

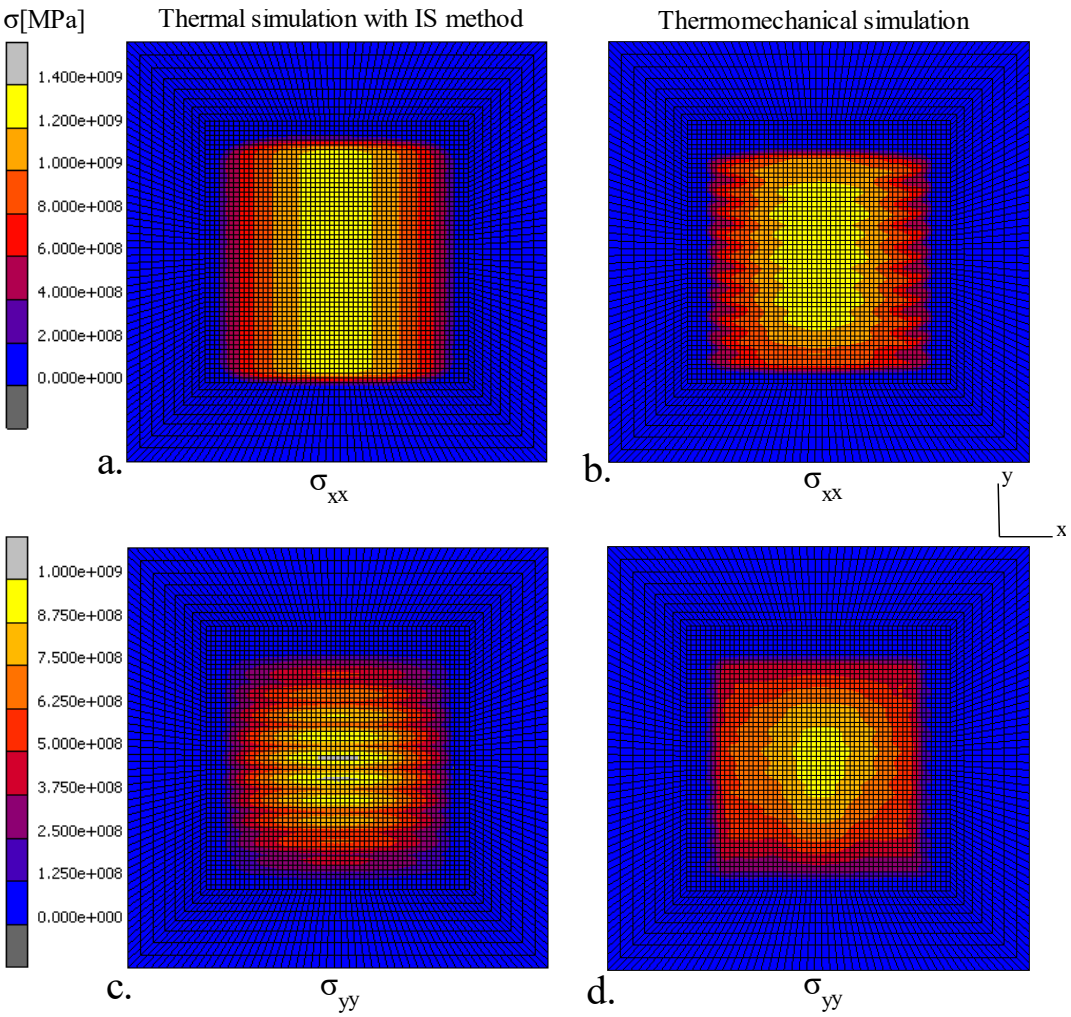

Figure 6-4: Comparison of ISM and thermomechanical solutions in terms of stress distributions. a. σ_{xx} from ISM, b. σ_{xx} from thermomechanical c. σ_{yy} from ISM, and d. σ_{yy} from thermomechanical solutions.

Figure 6-4 above shows a comparison between results from ISM and elastic-plastic thermomechanical analysis. Comparison was done using laser power as 160 W, scan spacing as 1 m/s, hatch spacing as 90 μm, and layer thickness as 40 μm. The stresses were residuals that were left after the material cooled down to steady-state temperature. Distributions and magnitudes of both longitudinal and transverse stresses that were from ISM results showed consistency with the thermomechanical solution.

To investigate the accuracy of the ISM on the prediction of stresses a study was done with ten different process parameter combinations as shown in Table 6-1. Error plots are shown in Figure 6-5. The average values of normal stresses in longitudinal and transverse directions were extracted from the surface of the hatched area. As explained before, the

longitudinal stresses were assumed to be the same for every parameter in the ISM theory. It can be seen that this assumption was reasonable based on the results of the thermomechanical solution. Moreover, it was found that transverse stresses had a correlation with the T_{max}, as formulated in the ISM. As a result, ISM predicted the residual stresses with a less than %10 error with respect to the thermomechanical solution, except for the variation of the parameter layer thickness. As mentioned in Chapter 4 before, variation in layer thickness directly alters the volume of the elements that were being deposited. ISM method uses only T_{max} to predict stresses and there was no significant change in T_{max} by alternation of the deposition volume, but stresses were highly influenced. Hence, the difference in the prediction of stresses between ISM and thermomechanical solution increased while the layer thickness was altered. On the other hand, by the ISM method computational time is decreased by six times compared to elastic-plastic thermomechanical simulation.

Table 6-1: Comparison of average stress results from ISM and thermomechanical solution for varying process parameters.

P	*v*	Δ*d*	Δ*h*	ISM	Thermo mech.	err.[%]	ISM	Thermo mech.	err.[%]
[W]	[m/s]	[µm]	[µm]	σxx[MPa]			σyy[MPa]		
160	1	90	40	1100	1066	+3.2	654	661	-1.1
190	1	90	40	1100	1082	+1.7	704	703	+0.1
220	1	90	40	1100	1085	+1.4	733	736	-0.4
160	0.6	90	40	1100	1082	+1.7	717	669	+7.2
160	1.2	90	40	1100	1060	+3.8	632	658	-4.0
160	1	75	40	1100	1082	+1.7	671	660	+1.7
160	1	100	40	1100	1080	+1.9	635	689	-7.8
160	1	90	30	1100	1174	-6.3	651	763	-14.7
160	1	90	50	1100	972	+13.2	665	578	+15.1
260	1.5	90	40	1100	1103	-0.3	718	788	-8.9

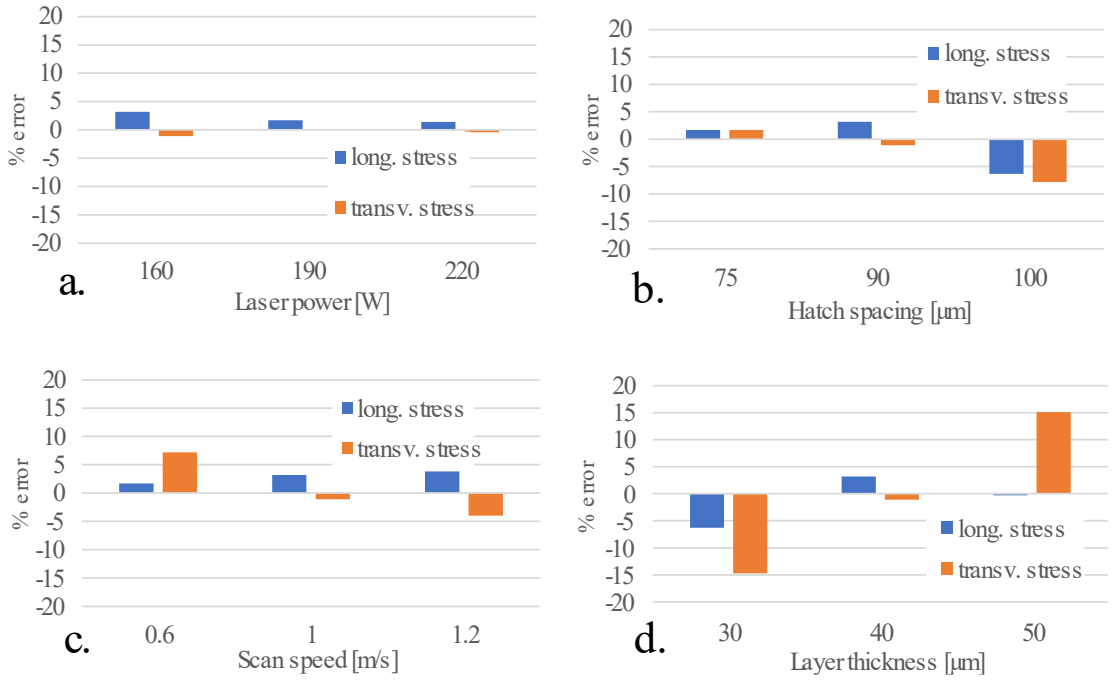

Figure 6-5: Error plots. a. laser power b. scan speed c. hatch spacing d. layer thickness

6.3 Summary

In this chapter, the theory of the original inherent strain method is discussed. Then, a modified stress-based version of the inherent strain method is described. This method used the same theory with the inherent strain method, however not inherent strains but residual stresses were directly predicted using the maximum temperatures that were achieved during the process. Thermomechanical results were used for calibration purposes and to extract distributions of stresses. Finally, a comparison was made between ISM and thermomechanical solution results. The study was done for ten different process parameter combinations. The maximum difference between the predicted stresses was %15.1 and it occurred while altering the layer thickness. For the other parameter combinations where layer thickness was constant and 40 μm, the maximum error was less than %10. By ISM computational effort was decreased by six times and also any numerical error that may occur in the elastic-plastic mechanical model was avoided since ISM only solves for thermal analysis to get the maximum temperatures. However, the method has some limitations. First of all, calibration may need to be done for each layer

thickness value separately, because stress variation while altering the layer thickness was independent of T_{max} but was directly related to the volume change. Secondly, the method could give reasonable results for a broad range of process parameters that are applicable for the process as shown in Table 6-1. On the other hand, deviation from thermomechanical solution would increase if exceptional process parameters are used. For instance, if the scan speed is increased to a very high value while keeping the other parameters constant, transverse stresses that are predicted from ISM would decrease drastically as a function of T_{max}. However, according to thermomechanical analysis, the influence of scan speed on transverse stresses is small and stresses would not decrease significantly. Yet, as long as the process parameters are chosen within the regular range as selected in this study, the ISM can be used to predict stresses with reasonable accuracy with respect to the thermomechanical solution.

7 CONCLUSIONS AND COMMENTS FOR FUTURE WORK

The Laser Powder Bed Fusion process is promising for industries where metal components with complex and customized designs are demanded. However, since it is relatively a recent manufacturing method when it is compared to conventional manufacturing techniques, optimization of process parameters demands further investigation. Efficient computational modeling of the process is critical to observe the relationship between process parameters and residual stresses that occur during the process.

In this thesis, the LPBF process was simulated with a computational finite element model. Material properties were used as a function of temperature and state to increase the accuracy of the model. Certain treatments were made to account for varying properties depending on the material phase (powder, liquid, and solid) as explained in Chapter 2. The size of the domain was selected for a meso-scale modeling approach with a moving volumetric heat source. The size of the elements in the mesh was decided based on a mesh sensitivity analysis. It was found that it is crucial to have a fine mesh around the heat-affected zone, otherwise, non-physical temperatures can be achieved around HAZ. The element size was selected also considering the computational time. Subroutines were written in FORTRAN® language to compute temperature and state dependent material properties during the analysis. Moreover, these user-defined routines were used to determine element activation, time step, heat source coordinates, and material model.

Accounting for surface heat losses is an issue in additive manufacturing simulations since most of the commercial finite element software requires a free surface in the model to define surface fluxes. However, with the layer by layer manufacturing, free surfaces always vary during the process. To resolve this difficulty a methodology was developed to represent surface heat fluxes as a volumetric input by using Gauss's (also known as divergence) theorem.

A parametric study was performed on a single layer deposition in which laser power, scanning speed, hatch spacing, and layer thickness parameters were examined. The results were compared in terms of melt pool sizes, maximum temperatures and residual stresses. According to the results, the dimensions of the melt pool were influenced most by the variation of laser power and scan speed. Melt pool dimensions almost uniformly changed in all directions with the laser power. On the other hand, while scan speed was altered, the aspect ratio of the melt pool was affected as well. Longitudinal residual stresses were found to be around the yield stress level for every studied process parameter combination. However, transverse stresses were increased when scan speed was decreased, or laser power was increased. Variation of layer thickness significantly influenced the stresses in both directions. Additionality, zigzag and uniform scan patterns were compared in terms of residual stress development. Although magnitudes were similar, there were deviations in terms of distributions of stresses between these scan strategies.

Based on the original inherent strain theory, a modified stress-based version was developed to predict stresses with solving only thermal analysis. Calibration was done using results from the thermomechanical solution. Results from fully thermomechanical solution and ISM were compared along ten different process parameter combinations. ISM predicted the stresses with a maximum of %15 error compared to the thermomechanical solution. Moreover, computational time was reduced by six times compared to the fully thermomechanical analysis.

For the future studies, presented stress based inherent strain method can be developed further to also include stress relaxation affect that occurs when a new layer is deposited on to the top of a layer. ISM uses only the maximum temperatures to predict stresses. In this study, these temperatures were gathered from the detailed meso-scale thermal simulation with a moving heat source. However, thermal history and these temperatures can be computed by using more simplified heat input assumptions such as line or layer heating methods. In these methods, heat input is given to a whole scan track or layer to reduce computational time drastically [59]. Hence, with a combination of these heat input methods and current ISM, prediction of stresses can be made through multi-layer part-scale simulations almost instantly.

BIBLIOGRAPHY

[1] "ISO/ASTM 52900: Additive manufacturing - General principles - Terminology," 2015.

[2] S. Singh, S. Ramakrishna, and R. Singh, "Material issues in additive manufacturing: A review," *J. Manuf. Process.*, vol. 25, pp. 185–200, 2017, doi: 10.1016/j.jmapro.2016.11.006.

[3] M. Tomlin and J. Meyer, "Topology Optimization of an Additive Layer Manufactured (ALM) Aerospace Part," *7th Altair CAE Technol. Conf. 2011*, pp. 1–9, 2011.

[4] D. Chen, S. Heyer, S. Ibbotson, K. Salonitis, J. G. Steingrímsson, and S. Thiede, "Direct digital manufacturing: Definition, evolution, and sustainability implications," *J. Clean. Prod.*, vol. 107, pp. 615–625, 2015, doi: 10.1016/j.jclepro.2015.05.009.

[5] S. Ford and M. Despeisse, "Additive manufacturing and sustainability: an exploratory study of the advantages and challenges," *J. Clean. Prod.*, vol. 137, pp. 1573–1587, 2016, doi: 10.1016/j.jclepro.2016.04.150.

[6] B. Berman, "3-D printing: The new industrial revolution," *Bus. Horiz.*, vol. 55, no. 2, pp. 155–162, 2012, doi: 10.1016/j.bushor.2011.11.003.

[7] I. Gibson, D. Rosen, B. Stucker, and M. Khorasani, *Additive Manufacturing Technologies*, 3rd ed. Springer International Publishing, 2021.

[8] T. Gornet, "History of Additive Manufacturing," pp. 1–24, 2017, doi: 10.4018/978-1-5225-2289-8.ch001.

[9] B. Wysocki, P. Maj, R. Sitek, J. Buhagiar, K. J. Kurzydłowski, and W. Świeszkowski, "Laser and electron beam additive manufacturing methods of fabricating titanium bone implants," *Appl. Sci.*, vol. 7, no. 7, pp. 1–20, 2017, doi: 10.3390/app7070657.

[10] I. Tolosa, F. Garciandía, F. Zubiri, F. Zapirain, and A. Esnaola, "Study of mechanical properties of AISI 316 stainless steel processed by 'selective laser melting', following different manufacturing strategies," *Int. J. Adv. Manuf. Technol.*, vol. 51, no. 5–8, pp. 639–647, 2010, doi: 10.1007/s00170-010-2631-5.

[11] C. Y. Yap *et al.*, "Review of selective laser melting: Materials and applications," *Appl. Phys. Rev.*, vol. 2, no. 4, 2015, doi: 10.1063/1.4935926.

[12] G. Totten, M. Howes, and T. Inoue, "Handbook of Residual Stress and Deformation of Steel," *ASM Int. Publ. USA*, pp. 417–444, 2002.

[13] J. Schijve, “Residual Stress,” in *Fatigue of Structures and Materials*, J. Schijve, Ed. Dordrecht: Springer Netherlands, 2009, pp. 89–104.

[14] P. Mercelis and J. P. Kruth, “Residual stresses in selective laser sintering and selective laser melting,” *Rapid Prototyp. J.*, vol. 12, no. 5, pp. 254–265, 2006, doi: 10.1108/13552540610707013.

[15] R. Andreotta, L. Ladani, and W. Brindley, “Finite element simulation of laser additive melting and solidification of Inconel 718 with experimentally tested thermal properties,” *Finite Elem. Anal. Des.*, vol. 135, no. July, pp. 36–43, 2017, doi: 10.1016/j.finel.2017.07.002.

[16] D. Rosenthal, *The theory of moving sources of heat and its application to metal treatments*. ASME, 1946.

[17] A. P. Mackwood and R. C. Crafer, “Thermal modelling of laser welding and related processes: A literature review,” *Opt. Laser Technol.*, vol. 37, no. 2, pp. 99–115, 2005, doi: 10.1016/j.optlastec.2004.02.017.

[18] S. W. Wen, P. Hilton, and D. C. J. Farrugia, “Finite element modelling of a submerged arc welding process,” *J. Mater. Process. Technol.*, vol. 119, no. 1–3, pp. 203–209, 2001, doi: 10.1016/S0924-0136(01)00945-1.

[19] Z. Zhang *et al.*, “3-Dimensional heat transfer modeling for laser powder-bed fusion additive manufacturing with volumetric heat sources based on varied thermal conductivity and absorptivity,” *Opt. Laser Technol.*, vol. 109, no. July 2018, pp. 297–312, 2019, doi: 10.1016/j.optlastec.2018.08.012.

[20] J. Irwin and P. Michaleris, “A Line Heat Input Model for Additive Manufacturing,” *J. Manuf. Sci. Eng. Trans. ASME*, vol. 138, no. 11, pp. 1–9, 2016, doi: 10.1115/1.4033662.

[21] S. S. Sih and J. W. Barlow, “The prediction of the emissivity and thermal conductivity of powder beds,” *Part. Sci. Technol.*, vol. 22, no. 4, pp. 427–440, 2004, doi: 10.1080/02726350490501682.

[22] X. Zhao, A. Iyer, P. Promoppatum, and S. C. Yao, “Numerical modeling of the thermal behavior and residual stress in the direct metal laser sintering process of titanium alloy products,” *Addit. Manuf.*, vol. 14, pp. 126–136, 2017, doi: 10.1016/j.addma.2016.10.005.

[23] L. Parry, I. A. Ashcroft, and R. D. Wildman, “Understanding the effect of laser scan strategy on residual stress in selective laser melting through thermo-mechanical simulation,” *Addit. Manuf.*, vol. 12, pp. 1–15, 2016, doi: 10.1016/j.addma.2016.05.014.

[24] E. R. Denlinger, M. Gouge, J. Irwin, and P. Michaleris, “Thermomechanical model development and in situ experimental validation of the Laser Powder-Bed Fusion process,” *Addit. Manuf.*, vol. 16, pp. 73–80, 2017, doi: 10.1016/j.addma.2017.05.001.

[25] C. Qiu, C. Panwisawas, M. Ward, H. C. Basoalto, J. W. Brooks, and M. M. Attallah, “Acta Materialia On the role of melt flow into the surface structure and porosity development during selective laser melting,” *Acta Mater.*, vol. 96, pp. 72–79, 2015, doi: 10.1016/j.actamat.2015.06.004.

[26] M. Zheng *et al.*, “A novel method for the molten pool and porosity formation modelling in selective laser melting,” *Int. J. Heat Mass Transf.*, vol. 140, pp. 1091–1105, 2019, doi: 10.1016/j.ijheatmasstransfer.2019.06.038.

[27] Z. Luo and Y. Zhao, “Efficient thermal finite element modeling of selective laser melting of Inconel 718,” *Comput. Mech.*, no. 0123456789, 2019, doi: 10.1007/s00466-019-01794-0.

[28] Z. Luo and Y. Zhao, “A survey of finite element analysis of temperature and thermal stress fields in powder bed fusion Additive Manufacturing,” *Addit. Manuf.*, vol. 21, no. December 2017, pp. 318–332, 2018, doi: 10.1016/j.addma.2018.03.022.

[29] P. Tan, F. Shen, B. Li, and K. Zhou, “A thermo-metallurgical-mechanical model for selective laser melting of Ti6Al4V,” *Mater. Des.*, vol. 168, p. 107642, 2019, doi: 10.1016/j.matdes.2019.107642.

[30] E. J. Schwalbach, S. P. Donegan, M. G. Chapman, K. J. Chaput, and M. A. Groeber, “A discrete source model of powder bed fusion additive manufacturing thermal history,” *Addit. Manuf.*, vol. 25, no. October 2018, pp. 485–498, 2019, doi: 10.1016/j.addma.2018.12.004.

[31] C. Li, J. F. Liu, and Y. B. Guo, “Efficient Multiscale Prediction of Cantilever Distortion by Selective Laser Melting,” *Proc. 27th Annu. Int. Solid Free. Fabr. Symp.*, pp. 236–246, 2016.

[32] Y. Ueda, Y. C. Kim, and M. G. Yuan, “A predicting method of welding residual stress using source of residual stress (report I): characteristics of inherent strain (source of residual stress)(mechanics, strength & structural design),” *Trans. JWRI*, vol. 18, no. 1, pp. 135–141, 1989.

[33] P. Promoppatum and V. Uthaisangsuk, “Part scale estimation of residual stress development in laser powder bed fusion additive manufacturing of Inconel 718,” *Finite Elem. Anal. Des.*, vol. 189, no. January, p. 103528, 2021, doi: 10.1016/j.finel.2021.103528.

[34] X. Liang, Q. Chen, L. Cheng, D. Hayduke, and A. C. To, “Modified inherent strain method for efficient prediction of residual deformation in direct metal laser sintered components,” *Comput. Mech.*, vol. 64, no. 6, pp. 1719–1733, 2019, doi: 10.1007/s00466-019-01748-6.

[35] M. Bugatti and Q. Semeraro, “Limitations of the inherent strain method in simulating powder bed fusion processes,” *Addit. Manuf.*, vol. 23, pp. 329–346, 2018, doi: 10.1016/j.addma.2018.05.041.

[36] Q. Chen *et al.*, “An inherent strain based multiscale modeling framework for simulating part-scale residual deformation for direct metal laser sintering,” *Addit. Manuf.*, vol. 28, no. December 2018, pp. 406–418, 2019, doi: 10.1016/j.addma.2019.05.021.

[37] T. Mukherjee, V. Manvatkar, A. De, and T. DebRoy, “Mitigation of thermal distortion during additive manufacturing,” *Scr. Mater.*, vol. 127, pp. 79–83, 2017, doi: 10.1016/j.scriptamat.2016.09.001.

[38] B. K. Panda and S. Sahoo, “Thermo-mechanical modeling and validation of

stress field during laser powder bed fusion of AlSi10Mg built part," *Results Phys.*, vol. 12, no. November 2018, pp. 1372–1381, 2019, doi: 10.1016/j.rinp.2019.01.002.

[39] H. Pohl, A. Simchi, M. Issa, and H. C. Dias, "Thermal stresses in direct metal laser sintering," *Proc. SFF Symp.*, pp. 366–372, 2001.

[40] L. S. Anderson, A. M. Venter, B. Vrancken, D. Marais, and J. Van Humbeeck, "Investigating the Residual Stress Distribution in Selective Laser Melting Produced Ti-6Al-4V using Neutron Diffraction," *Mech. Stress Eval. by Neutron Synchrotron Radiat.*, vol. 4, pp. 73–78, 2018, doi: 10.21741/9781945291678-11.

[41] T. Mukherjee, W. Zhang, and T. DebRoy, "An improved prediction of residual stresses and distortion in additive manufacturing," *Comput. Mater. Sci.*, vol. 126, 2017, doi: 10.1016/j.commatsci.2016.10.003.

[42] J. Robinson, I. Ashton, P. Fox, E. Jones, and C. Sutcliffe, "Determination of the effect of scan strategy on residual stress in laser powder bed fusion additive manufacturing," *Addit. Manuf.*, vol. 23, no. February, pp. 13–24, 2018, doi: 10.1016/j.addma.2018.07.001.

[43] Special Metals, "IN718 Datasheet," *Special Metals Corporation*, 2007. [Online]. Available: www.specialmetals.com. [Accessed: 06-Feb-2021].

[44] K. C. Mills, "Ni - IN 718," in *Recommended Values of Thermophysical Properties for Selected Commercial Alloys*, K. C. Mills, Ed. Woodhead Publishing, 2002, pp. 181–190.

[45] G. A. Greene, C. C. Finfrock, and T. F. Irvine, "Total hemispherical emissivity of oxidized Inconel 718 in the temperature range 300–1000°C," *Exp. Therm. Fluid Sci.*, vol. 22, no. 3, pp. 145–153, 2000, doi: https://doi.org/10.1016/S0894-1777(00)00021-2.

[46] D. Deng and S. Kiyoshima, "Numerical simulation of residual stresses induced by laser beam welding in a SUS316 stainless steel pipe with considering initial residual stress influences," *Nucl. Eng. Des.*, vol. 240, no. 4, pp. 688–696, 2010, doi: 10.1016/j.nucengdes.2009.11.049.

[47] G. R. Hadley, "Thermal conductivity of packed metal powders," *Int. J. Heat Mass Transf.*, vol. 29, no. 6, pp. 909–920, 1986, doi: 10.1016/0017-9310(86)90186-9.

[48] Y. S. Lee and W. Zhang, "Modeling of heat transfer, fluid flow and solidification microstructure of nickel-base superalloy fabricated by laser powder bed fusion," *Addit. Manuf.*, vol. 12, pp. 178–188, 2016, doi: 10.1016/j.addma.2016.05.003.

[49] K. H. Leitz, P. Singer, A. Plankensteiner, B. Tabernig, H. Kestler, and L. S. Sigl, "Multi-physical simulation of selective laser melting," *Met. Powder Rep.*, vol. 72, no. 5, pp. 331–338, 2017, doi: 10.1016/j.mprp.2016.04.004.

[50] J. Goldak, A. Chakravarti, and M. Bibby, "A new finite element model for welding heat sources," *Metall. Trans. B*, vol. 15, no. 2, pp. 299–305, 1984, doi: 10.1007/BF02667333.

[51] N. Dunne, Fionn and Petrinic, *Introduction to Computational Plasticity*. Oxford Univ. Press, UK, 2005.

[52] R. D. Cook, D. S. Malkus, M. E. Plesha, and R. J. Witt, *Concepts and Applications of Finite Element Analysis*. Hoboken, NJ, USA: John Wiley & Sons, Inc., 2007.

[53] M. A. Bhatti, *Advanced Topics in Finite Element Analysis of Structures: With Mathematica and MATLAB Computations*. USA: John Wiley & Sons, Inc., 2006.

[54] X. Fung, Yuen-cheng and Tong, Pin and Chen, *Classical and computational solid mechanics*. World Scientific Publishing Company, 2017.

[55] L. Scime and J. Beuth, "Melt pool geometry and morphology variability for the Inconel 718 alloy in a laser powder bed fusion additive manufacturing process," *Addit. Manuf.*, vol. 29, no. August, p. 100830, 2019, doi: 10.1016/j.addma.2019.100830.

[56] E. GmbH, "Corporate website," *2021*. [Online]. Available: http://www.eos.info/en. [Accessed: 17-Feb-2021].

[57] A. V. Gusarov, M. Pavlov, and I. Smurov, "Residual stresses at laser surface remelting and additive manufacturing," *Phys. Procedia*, vol. 12, no. PART 1, pp. 248–254, 2011, doi: 10.1016/j.phpro.2011.03.032.

[58] Y. Luo, H. Murakawa, and Y. Ueda, "Prediction of Welding Deformation and Residual Stress by Elastic FEM Based on Inherent Strain (Report I) : Mechanism of Inherent Strain Production(Mechanics, Strength & Structure Design)," *Trans. JWRI*, vol. 26, pp. 49–57, 1996.

[59] Y. P. Yang, M. Jamshidinia, P. Boulware, and S. M. Kelly, "Prediction of microstructure, residual stress, and deformation in laser powder bed fusion process," *Comput. Mech.*, vol. 61, no. 5, pp. 599–615, 2018, doi: 10.1007/s00466-017-1528-7.